

GEFENOL Summer School on Statistical Physics of Complex Systems
Hard particle models in 2D: From soft matter to granular media

Enrique Velasco and Yuri Martínez-Ratón

Contents

1 Phenomenology of hard particles and Density-Functional Theory **3**

1.1 Introduction . . . 3
1.2 Connection with fundamental geometry . . . 5
1.3 Role as a potential energy model for particle interactions . . . 5
1.4 Anisotropic particle models . . . 7
1.5 Packing fraction . . . 8
1.6 Low density limit . . . 8
1.7 Introduction to simple models for fluids, liquid crystals and crystals . . . 9
1.8 Density-functional Theory: exactly solved hard-body model in 1D . . . 17

2 Scaled-Particle Theory in 2D. Monte Carlo simulation **20**

2.1 A working example: confined hard rods in 1D . . . 24
2.2 Dimensional crossover . . . 24
2.3 Density functional for the 2D Zwanzig model . . . 28
2.4 Scaled particle theory . . . 30
2.5 Fluid of hard rectangles (HR) . . . 31
2.6 Fluid of hard isosceles triangles (HT) . . . 35
2.7 Monte Carlo method for anisotropic hard particles . . . 37
2.8 N-particle system of hard-rod particles . . . 40

3 Vibrated granular monolayers and elastic theory **42**

3.1 Introduction . . . 42
3.2 Elastic Theory for 2D nematics . . . 42
3.3 Experiments on vertically vibrated monolayers of granular anisotropic particles . . . 47

Abstract

Hard-body models have played an important role in the understanding of the properties of matter, especially of simple liquids and crystals. They are central to statistical mechanics and condensed-matter physics. At present they continue to generate a great interest in the areas of soft matter and complex fluids as models for colloids, liquid crystals and granular matter. In this course we present an introduction to the classical statistical mechanics of hard-body models and their use in condensed matter physics to represent the phenomenology of both equilibrium and nonequilibrium complex fluids and granular matter. The emphasis is on 2D systems. Both theoretical methods, as long as computational approaches, are discussed. Numerical exercises are suggested.

Preface

The course provides an overview of hard-particle models and their applications in condensed-matter physics as simplified, yet remarkably realistic, representations of the phenomenology of equilibrium and nonequilibrium complex fluids and granular materials. Particular emphasis is placed on two-dimensional systems. Both theoretical and computational approaches are discussed, and a number of numerical exercises are proposed throughout the course.

The course is organized around the following main topics:

- Geometry as a source of physics. The geometry embodied in hard-body models gives rise to a rich variety of physical phenomena. Excluded-volume interactions govern the behaviour of equilibrium hard-particle systems and drive phase transitions, orientational and positional ordering, and the emergence of rigidity and elasticity in partially or fully ordered phases.

- Entropy as an ordering mechanism. In hard-particle systems, entropy is the dominant thermodynamic potential. Contrary to the common perception of entropy as a source of disorder, it can promote the spontaneous formation of ordered phases, explaining fundamental phenomena such as crystallization and the orientational ordering of liquid crystals.

- Granular matter and nonequilibrium physics. Granular systems can often be successfully modelled as assemblies of hard particles. They exhibit a wealth of nonequilibrium phenomena, including dissipation, the breaking of detailed balance, strong dependence on initial conditions, and metastability. Under appropriate driving conditions, however, granular layers may display phase behaviour that closely resembles that of equilibrium systems.

1 Phenomenology of hard particles and Density-Functional Theory

In this lecture, we introduce hard-body models as simple yet powerful representations of particle interactions in a wide range of condensed-matter systems, including simple and complex fluids, colloidal suspensions, liquid crystals, crystalline solids, and granular materials. For a general review of hard-body models and theories in the context of liquid crystals see Ref. [1].

1.1 Introduction

Hard-body models are the simplest possible description of interacting particles. The only acceptable configurations are those in which the particles do not overlap (Fig. 1). For all such configurations, the potential energy is identically zero, so the interaction is defined entirely by the geometry of the particles. As a result, the kinetic energy provides the only energetic contribution. In a classical system at thermal equilibrium, however, the kinetic energy is trivial and independent of the particle configuration. Consequently, the equilibrium properties of hard-body systems are determined entirely by entropy.

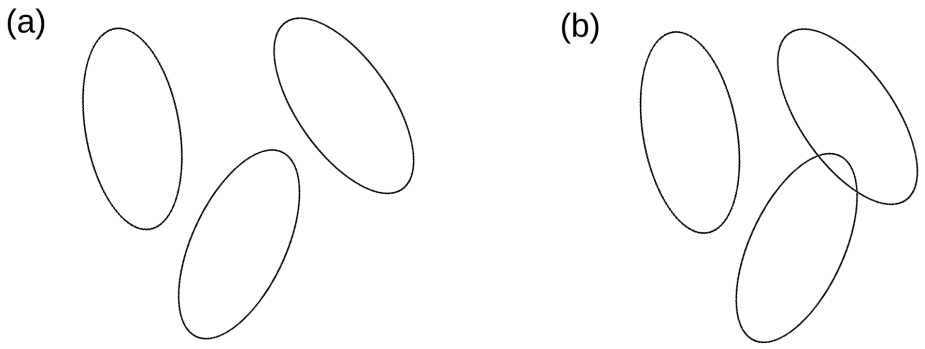


Figure 1: A system of three hard particles. (a) Allowed configuration: none of the particles overlaps with the others. (b) Nonallowed configuration: two of the particles overlap.

Hard-particle models have revealed one of the deepest principles in condensed-matter physics:

Collective order does not require energetic interactions. Geometry alone can organize matter.

We will see that this important principle can be quantified in terms of an important geometric concept, that of *excluded volume*, see Fig. 2. The same excluded-volume principles connect seemingly different fields: liquid crystals, colloidal suspensions, granular media, jamming, glasses, and random packings.

In this sense, hard anisotropic particles form a common language that link statistical mechanics and geometry. They provide perhaps the clearest setting in all of condensed-matter physics in which shape is the interaction, and understanding how geometric properties determine entropy remains one of the central themes of modern soft condensed matter and granular physics. This course tries to give a flavour of these concepts.

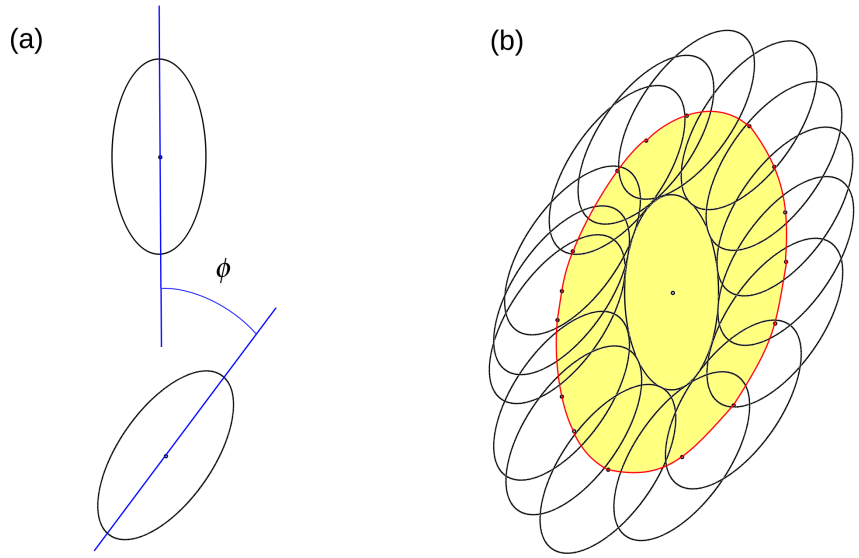


Figure 2: Excluded volume: every particle excludes the centre of mass of the other particles from a volume surrounding the particle. (a) Two particles with relative orientation of their long axes given by the angle ϕ. (b) The volume excluded by one particle to the centre of mass of the other particle is given by the yellow area. Violation of the excluded volume leads to nonallowed configurations.

Hard-body interactions give rise to several phenomena that are, at first sight, rather counterintuitive. It is commonly believed that ordered phases of matter arise because neighbouring particles lower their energy by occupying attractive potential wells, leading generally to perfectly ordered particle arrangements. In this view, the Hamiltonian of a system of N classical particles,

$$\mathcal{H} = \sum_{i=1}^{N} \frac{|\boldsymbol{p}_i|^2}{2m} + U(\boldsymbol{r}_1, \cdots, \boldsymbol{r}_N), \tag{1}$$

is expected to attain its minimum in an ordered configuration, the ordering being driven by the potential energy function U.

Hard-body systems are fundamentally different. The interaction potential takes only two values: it is zero when particles do not overlap and infinite when they do. There are therefore no attractive wells capable of favouring one configuration over another. From an energetic point of view, all acceptable configurations are equivalent.

The explanation for the emergence of ordered phases is instead provided by statistical mechanics. Thermal equilibrium is determined not by the internal energy alone, but by the free energy. In hard-body systems, where the internal energy is identical for all allowed configurations, the equilibrium behaviour is governed entirely by entropy. As we shall see later, entropy (usually associated with disorder) can, somewhat paradoxically, become the driving force behind the formation of highly ordered phases.

1.2 Connection with fundamental geometry

There is a deep connection between hard-particle systems and geometry. The key geometric measures of a particle include: the volume v, the area a, the mean curvature H and the Euler characteristics χ. All of these parameters appear naturally in the important theories of hard-body systems, namely scaled-particle theory and fundamental-measure theory. An important insight is that many thermodynamic properties depend only on a small set of geometric measures, which reveals a relation between differential geometry and statistical mechanics.

One the greatest achievements in hard-particle theory is the density functional theory developed by Y. Rosenfeld, called the *Fundamental Measure Theory* (FMT) [2]. This theory writes the excess free energy in terms of geometric measures of particles, and is extraordinarily accurate for hard spheres. There have been extensions for rods, ellipsoids, more general convex bodies and also mixtures. The idea of the theory is that it incorporates geometric information into thermodynamics. FMT is considered one the most elegant density-functional theories ever developed.

1.3 Role as a potential energy model for particle interactions

A realistic interaction potential between two atoms or molecules with approximately spherical symmetry is shown in Fig. 3(a). Such potentials typically consist of two distinct parts: a steep short-range repulsion and a longer-range attraction that decays to zero as the intermolecular distance increases, usually following a power law determined by the nature of the interaction (most commonly van der Waals forces). A classical example is the well-known Lennard–Jones potential.

Hard-body models correspond to the limiting case in which only the repulsive core of the interaction is retained, Fig. 3(b). In many atomic and molecular systems, this repulsive contribution plays the dominant role in determining the local packing of particles and, in many cases, even the global structure and symmetry of the material. The attractive contribution can then often be incorporated as a perturbation to the hard-body reference system.

Hard-body models, however, are much more than convenient reference systems. In many physical systems they provide an accurate description of the complete interaction because attractive forces are either negligible or effectively irrelevant. This is the case, for example, in certain globular proteins, whose interactions are well approximated by excluded-volume effects, and in colloidal suspensions with very short-ranged attractions. Typical colloidal particles have sizes of the order of one micrometre, whereas the range of the attractive van der Waals interaction remains on the nanometre scale. Although integrating the van der Waals forces over the particle volumes results in a strong attraction, its range is still extremely short compared with the particle diameter. Consequently, the behaviour of such systems is often governed primarily by excluded-volume interactions and can be described remarkably well by hard-body models.

The simplest model for spherically symmetric interactions is the hard-sphere (HD) model. It may be defined in 1D, 2D, 3D or even higher dimensions. The pair interaction potential $\phi(r)$ as

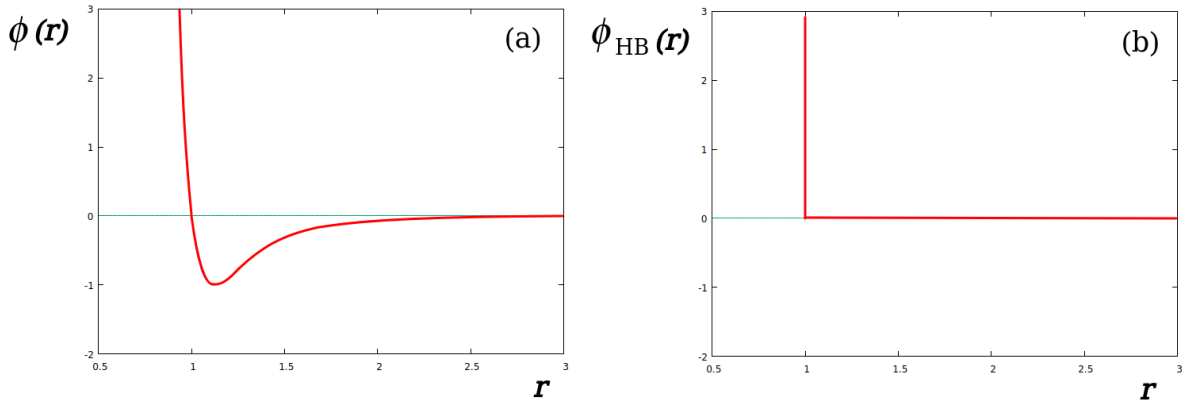


Figure 3: (a) Realistic pair potential between two spherically-symmetric atoms or molecules: the Lennard-Jones potential. (b) The hard-sphere potential, corresponding to two interacting spheres of diameter σ (the contact distance bewteen the spheres). This model can be generalised to hard anisotropic particles by making the contact distance to be a function of the particle orientations and of the relative orientation between the centres of mass.

a function of the interparticle distance r is

$$\phi(r) = \begin{cases} \infty, & r < \sigma \\ 0, & r > \sigma \end{cases} \tag{2}$$

The only characteristic parameter of the model is a length, σ, the diameter of the hard spheres. Hard-sphere interactions are pairwise by definition, so that the total potential energy function is

$$U(\boldsymbol{r}_1, \cdots, \boldsymbol{r}_N) = \sum_{i=1}^{N} \sum_{j>i} \phi(r_{ij}), \tag{3}$$

where the sums run over all distinct pairs, $r_{ij} = |\boldsymbol{r}_i - \boldsymbol{r}_j|$, and $\{\boldsymbol{r}_i\} = \{\boldsymbol{r}_1, \cdots, \boldsymbol{r}_N\}$ are the positions of the particles.

In systems subject to thermal fluctuations in equilibrium (driven by a Boltzmann distribution at temperature T), the model has a trivial dependence on T. To see this, consider the partition function of a system of N spheres, which will be represented by

$$Z_N = \mathrm{Tr}_{\mathrm{clas}} e^{-\beta U(\boldsymbol{r}_1, \cdots, \boldsymbol{r}_N)}, \tag{4}$$

where $\mathrm{Tr}_{\mathrm{clas}}$ is the classical trace, a conveniently normalised integral over momenta and positions, weighted by the Boltzmann factor of each configuration, with $\beta \equiv (kT)^{-1}$. Note that $U = 0$ for nonoverlapping configurations of the spheres, while $U = \infty$ for configurations where at least two spheres do overlap. The result is that Z_N: (i) is a sum of zeros and ones, and (ii) does not depend on T. The Helmholtz free energy $F = -kT \log Z_N = E - TS$ is

$$F = T \times (\text{function that depends on the density and particle geometry}) . \tag{5}$$

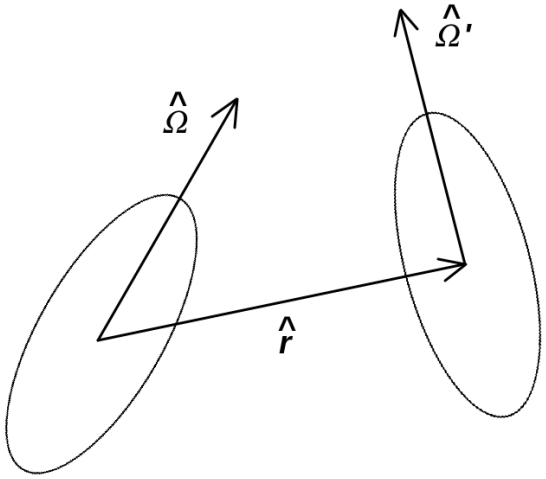


Figure 4: Angles defining the interaction between two anisotropic hard bodies with symmetry of revolution.

The equilibrium energy $E = \langle E_c + U \rangle$ (where E_c is the kinetic energy) is again proportional to T:

$$E = \langle E_c \rangle + \langle U \rangle = \frac{3}{2} NkT + 0 = \frac{3}{2} NkT. \tag{6}$$

The function in parenthesis above is basically the entropy:

$$F = NkT \left(\frac{3}{2} - S \right). \tag{7}$$

The temperature prefactor is irrelevant for phase behaviour, and we conclude that, in systems of hard particles, *equilibrium properties are governed by entropy alone*, and that the equilibrium state follows by maximizing entropy.

1.4 Anisotropic particle models

The discovery over the last decades that systems of model hard particles can exhibit a large variety of phases, from uniform phases to phases with partial and full order, is one of the most interesting recent advances in condensed-matter physics. The fact that particles that do not attract to each other are capable of forming complex phases with nontrivial symmetries has revolutionised the role of entropy in condensed matter and our view of entropy as a *disordering agent*: entropy alone, through its maximization, can drive order in subtle ways, as we will discover in the coming sections.

Hard spheres in various dimensionalities are not the only application of hard-body models. They have been generalised to nonspherical particles, or combinations of particles, to describe complex systems based on molecular or colloidal particles. A simple way to define anisotropic particle models is through the pair potential contact distance σ. By assuming a dependence of σ on the angles involved in the problems, we can generate different interactions. For bodies with symmetry of revolution about one axis, these angles can be described in terms of three unit vectors,

see Fig. 4: $\hat{\boldsymbol{r}}$, the relative vector joining the centres of mass of two particles, $\hat{\boldsymbol{\Omega}}$, the vector along the long axis of one particle, and $\hat{\boldsymbol{\Omega}}'$, the vector along the long axis of another particle. We thus have $\sigma = \sigma(\hat{\boldsymbol{r}}, \hat{\boldsymbol{\Omega}}, \hat{\boldsymbol{\Omega}}')$. This contact distance can be used in different models, for instance, the hard-sphere model, to generate a hard-body anisotropic pair potential. A famous model for this contact distance is given by the Gay-Berne potential, a generalisation of the Lennard-Jones potential where the contact distance is anistropic. With the same model for contact distance we can generate the so-called Hard-Gaussian Overlap model, which is very close to the hard-ellipsoid model consisting of nonoverlapping ellipsoid of revolution. Biaxial molecules can also be generated using this technique.

Much of this course will consider two-dimensional (2D) models. For example, in 2D, hard particles with elliptical shape or hard ellipses (HE), can describe nematic liquid-crystalline ordering. Other popular models are: hard rectangles (HR), hard discorectangles (HDR, a rectangle ended by semicircles at each end), etc. In 3D we have hard ellipsoids, hard cylinders, hard spherocylinders, hard boards, and other models with nonconvex shapes. In turn, these particles can be taken as units and combined into long assemblies to describe polymers, biological molecules, etc. The variety and flexibility of hard models are very large.

1.5 Packing fraction

Since temperature is not an important parameter in hard-body systems, the only relevant thermodynamic variable is the number density $\rho = N/V$, where N is the number of particles and V the volume of the system. This has dimensions of volume^{-1}. A more convenient quantity for hard-body systems is the *packing fraction*. This is defined as

$$\phi = \frac{\text{Volume occupied by particles}}{\text{Total volume available}} = \frac{Nv}{V} = \rho v. \tag{8}$$

Therefore, the packing fraction is simply equal to the density multiplied by the particle volume, which makes the density dimensionless. Note that $0 \leq \phi \leq 1$, with $\phi = 1$ representing the highest possible packing where the whole space is occupied by particles. Obviously this is not possible for all except a few class of particles which are volume-filling: cubes, rectangular prisms, ans some other polyhedra. In general there is a maximum value for packing fraction, $\phi_{\max} < 1$, called *close-packed limit*. For example, for hard spheres of diameter σ, we have $\phi_{\max} = \pi\rho\sigma^3/6 = 0.64...$ We will briefly review these problems later in the course.

1.6 Low density limit

We know from statistical mechanics that all thermodynamic properties of a system may be expanded in terms of the density via the *virial expansion*. For the pressure p,

$$\frac{p}{\rho k_B T} = 1 + B_2\rho + \cdots, \quad B_2 = -\frac{1}{2}\int d\boldsymbol{r} \int d\hat{\boldsymbol{\Omega}}_1 \int d\hat{\boldsymbol{\Omega}}_2 f(\boldsymbol{r},\hat{\boldsymbol{\Omega}}_1,\hat{\boldsymbol{\Omega}}_2), \tag{9}$$

where B_2 is the *second virial coefficient*, which gives the leading linear behaviour in density beyond the ideal contribution. B_2 collects the effects of two-body correlations, while higher-order virial coefficients B_n, $n > 2$, contain contributions from three-, four-, etc. particle correlations.

f is the Mayer function

$$f(\boldsymbol{r},\hat{\boldsymbol{\Omega}}_1,\hat{\boldsymbol{\Omega}}_2) = e^{-\Phi(\boldsymbol{r},\hat{\boldsymbol{\Omega}}_1,\hat{\boldsymbol{\Omega}}_2)/k_BT} - 1, \tag{10}$$

and those high-order terms can also be expressed as integrals of products of Mayer functions. For hard bodies, $f = 0$ for nonoverlapping configurations of the two particles, while $f = -1$ for configurations where the two particles overlap. Note that here it is the overlapping configurations which contribute to the pressure! Here we see again the deep geometric relation of hard particles with thermodynamics: the dual configuration space of overlapping configurations determine some properties, while the partition function only contains nonoverlapping configurations.

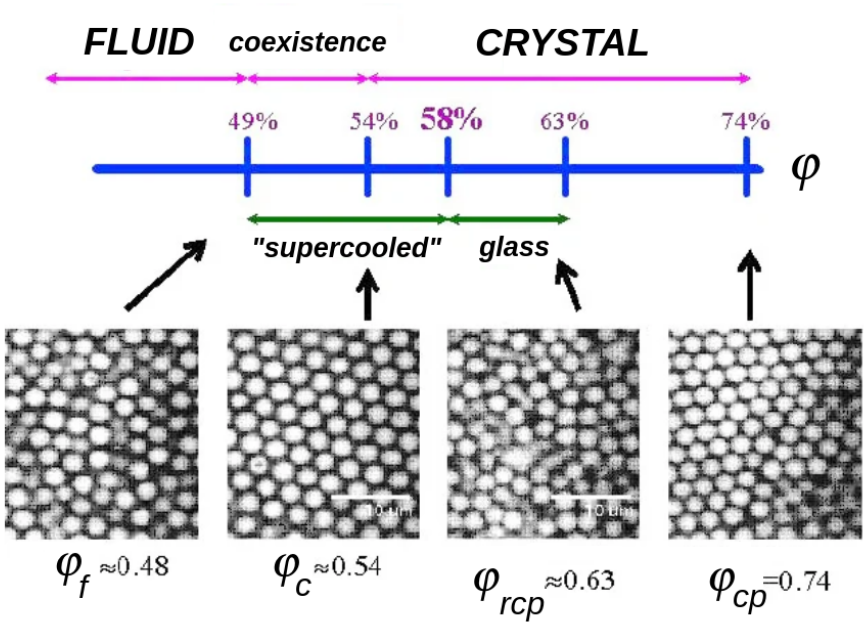


Figure 5: Phase diagram of the HS model. The only relevant parameter is density, or packing fraction φ. The fluid phase coexist with a crystal phase in the range $\varphi \in [0.48,0.54]$. The highest packing fraction $\varphi_{\rm cp}$ (close packing fraction) is 0.76, corresponding to an fcc crystal structure. In colloidal systems that can be modelled in terms of the HS model, there is a kinetically-arrested glass state with a maximum packing at ~ 0.63 (random close packing).

1.7 Introduction to simple models for fluids, liquid crystals and crystals

In this section we review the phases and the phase diagrams of some of the most popular hard-body models, beginning with the hard-sphere model.

Hard spheres (HS). This is the most basic nontrivial interaction hard-body model. The phase diagram only depends on the density or packing fraction ϕ. The model exhibits a phase transition from a fluid phase to a crystal phase, with $\phi = 0.496$ and 0.548 for the coexisting fluid and crystal phases, respectively. The transition is of first order, meaning that there is a discontinuity in density at the transition (thermodynamically there is a discontinuity in the derivative of the free energy). Fig. 5 displays the phase diagram of the hard-sphere model. The crystal phase is a lattice with fcc symmetry. Obviously the crystal of HS can only exist if it is subject to

some pressure. So a system of 3D hard spheres at some temperature T may exhibit two possible phases: a fluid and a crystal with fcc (face-centred cubic) symmetry. While the fluid phase is easy to understand, the crystal is less so. How could a collection of purely repulsive spheres decide to organize into an ordered configuration by maximizing its entropy?

The HS model explains the fluid-crystal transition in terms of entropy and the competition between two types of entropy. One is the ideal-gas entropy, which tends to disorder the system. The other is the excess entropy, associated to the interactions, which tends to order the system. The competition is won by the ideal entropy in the fluid, and by the interaction entropy in the crystal. Note that the equilibrium phase results by *maximizing* the entropy. The fact that the crystal is favoured by a maximum in the interaction entropy requires an explanation.

The answer is not a trivial one, and it took some time to understand it, both through a mixture of simulation and theoretical work. An intuitive argument is the following. The interaction entropy is governed basically by excluded volume. In a system of many spheres what counts is the space available to a sphere which is left by the others. The volume of this space, $\mathcal{V}$, is directly related to the entropy (via the log of the volume, or number of continuous states, available). A maximum volume gives a maximum entropy through the relation $S \sim \log \mathcal{V}$. It turns out that this volume is maximum for the ordered configuration of spheres, as in this configuration an average sphere has more freedom to wander around its cage (see Fig. 6).

A slightly different argument is given by classical density-functional theory (DFT), the natural tool to describe hard-body systems. Essentially, the entropy S has two contributions: an ideal entropy whose maximum drives the system towards a disordered state, and an interaction entropy, genuinely originating in the hard-body interaction, which is a maximum for the ordered state. The competition between these two entropic parts leads to a fluid phase at low density, and to a crystal phase at high density, with a first-order transition in between.

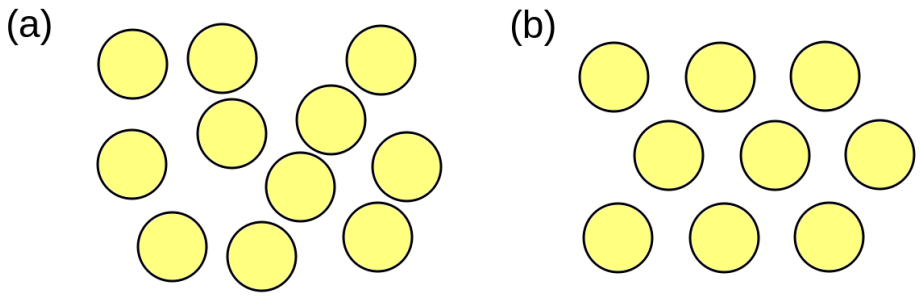


Figure 6: At the same density, an ordered crystal configuration of hard spheres may be such that the free volume of a sphere is larger than that in the disordered fluid configuration.

An important aspect of the HS model is that at present there are many different experimental realizations of almost perfect hard spheres. Fig. 7 shows an example of a crystal made of colloidal spheres made of polymer. We can see the perfect structure of the sample, which corresponds to an fcc crystal. The possibility to synthetize these and other types of particles have again brought the hard-body models at the forefront of research in condensed matter physics.

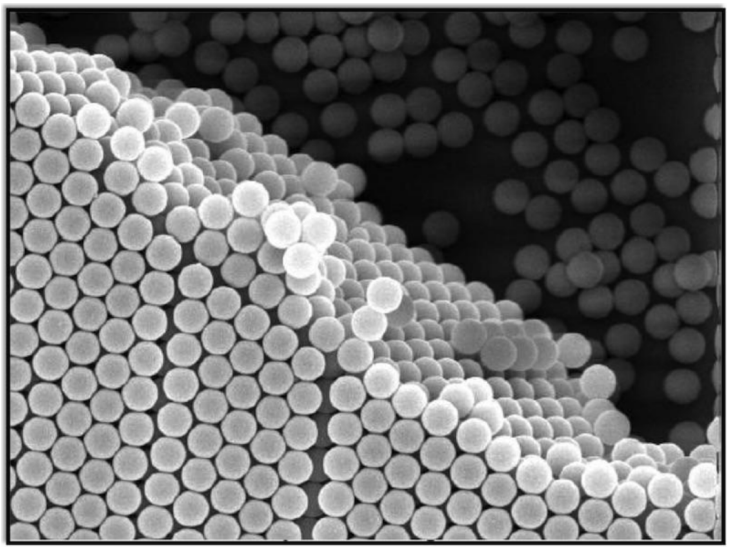


Figure 7: A crystal phase of polymer colloidal spheres [3].

Mixtures of hard spheres. The HS model can also be used to explain part of the phenomenology of mixtures of spheres, i.e. spheres with different diameters σ_1 and σ_2. Normally one considers the additive case, where the cross interaction is simply a hard-sphere model. If σ_{ij} is the equivalent diameter for the interaction between species i and j, we have

$$\sigma_{11} = \sigma_1, \quad \sigma_{22} = \sigma_2, \quad \sigma_{12} = \frac{1}{2}(\sigma_1 + \sigma_2). \tag{11}$$

A crucial parameter in mixtures is the composition,

$$x = \frac{N_1}{N_1 + N_2}. \tag{12}$$

where N_1 and N_2 are the numbers of spheres of the two species, respectively.

A useful way to view additive binary hard-sphere mixtures is that they are the simplest entropy-only model for colloids with two diameters, $q = \sigma_2/\sigma_1$. Again there is no energy scale: phase behaviour is controlled by total packing fraction φ, composition x, and size ratio q.

Fluid mixtures can be analysed in terms of the generalised Carnahan–Starling equation of state, which is standard in the theory of liquids. For moderate size asymmetry, mixtures mainly alter the usual hard-sphere freezing transition. Monodisperse spheres freeze at $\varphi = 0.494$ and melt at $\varphi = 0.545$. Adding a second size can either frustrate crystallization or stabilize binary crystals, depending on q and composition. Fig. 8 (left) shows different crystal structures than can be stabilized in mixtures. Results of Monte Carlo simulations indicate that the most stable structures have the form AB_2 in the range $0.76 \leq q \leq 0.84$, instead of the expected CsCl structure [4]. Other ratios may lead to frustrated crystal phases or more complicated arrangements.

The long-standing question is whether purely additive hard-sphere mixtures show a stable fluid-fluid demixing transition. Many integral-equation or approximate free-energy theories predicted demixing at high asymmetry, but simulations and effective-Hamiltonian approaches generally

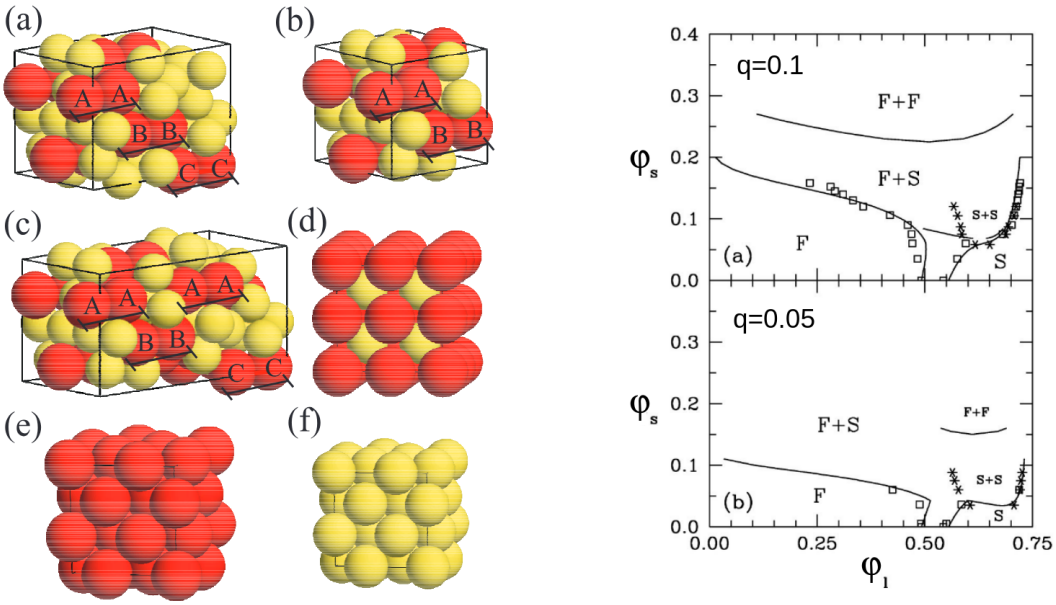


Figure 8: Left: possible crystal structures for mixtures of hard spheres. fcc crystals of the pure species are shown at the bottom [4]. Right: phase diagram of two mixtures with $q = 0.1$ and 0.05, using the Asakura-Oosawa effective potential and DFT theory [5]. The fluid-fluid transition is always metastable with respect to the fluid-crystal transition.

find that, for additive hard spheres, any fluid–fluid separation is metastable or preempted by fluid–crystal coexistence. Dijkstra et al. [6] found a metastable fluid–fluid transition for $q < 0.1$, while the stable transition is the fluid–solid transition. These findings have also been obtained using Density-Functional Theory [5], see Fig. 8 (right).

Entropic forces and torques. A particularly relevant case is that of the depletion interaction. This is a collective interaction of entropic origin. It results when the difference in size between the two components is large. Then, two spheres of the larger component may feel an attractive "interaction" when they are very closely separated (separation on the order of the size of the small component), due to an uncompensated balance between the pressure on the outside region of the spheres and the interior pressure, due to the absence of small spheres in the region bewteen the large spheres. The force is not direct but can be explained in terms of entropy: when the excluded volumes of two large spheres overlap, solvent spheres have more free space to move around (see Fig. 9), so that their entropy increases and the free energy decreases. This can be viewed as an effective attractive force that lowers the free energy.

One area where depletion forces are at work is macromolecular crowding effects in the interior of a cell. Proteins and nucleic acids are found in high densities in the cytoplasm. Depletion attraction helps these molecules self-assemble into larger functional structures, ranging from the cytoskeleton to chromatin loops, without requiring specific chemical bonding. Also, the functioning of a protein involves binding ligands to specific attachment points in the protein. This docking process is believed to be very efficient because of depletion forces and torques (the equivalent phenomenon when orientations of elongated molecules species are involved).

2D freezing. The freezing of hard discs (hard spheres in 2D) is particularly interesting. The

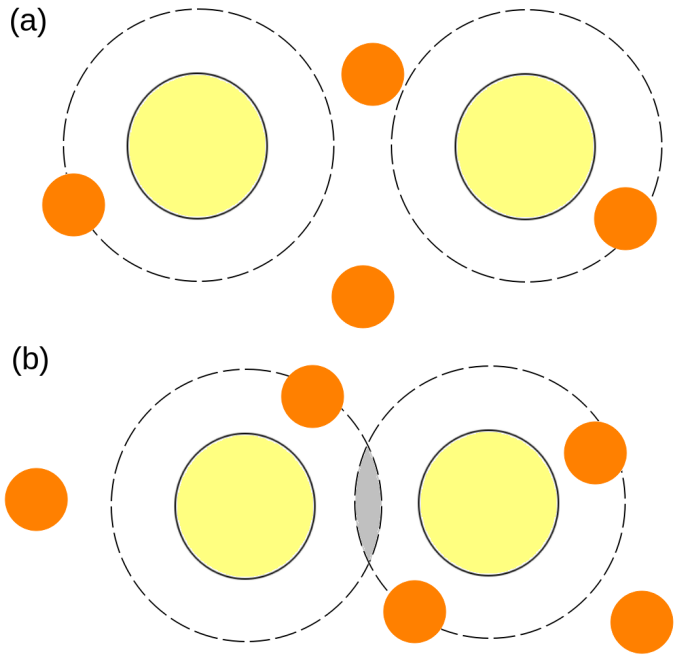


Figure 9: (a) Two large nonoverlapping hard spheres with their respective excluded volumes, surrounded by smaller spheres. (b) When sufficiently close, the total free volume available to the small-sphere species is enlarged because of the overlap between the two excluded volumes, which causes the entropy to increase, which can be interpreted as an effective attractive force of entropic origin.

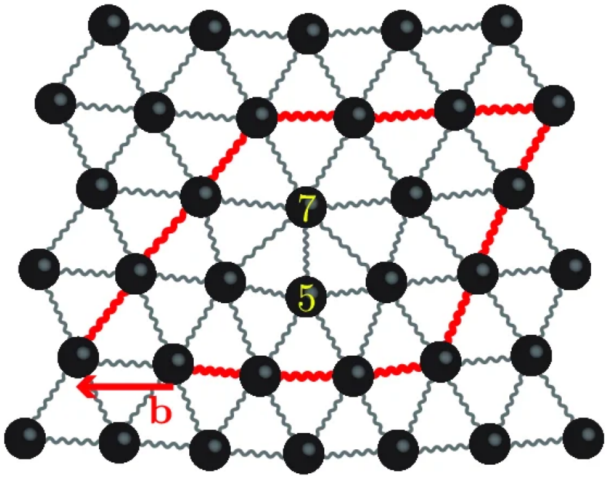


Figure 10: A dislocation in a triangular lattice: a pair of bound disclinations. The Burgess vector of the dislocation is shown with an arrow: encircling the disclination by the same multiple of lattice units in each direction the returning point is not the same. Translation symmetry is thus disrupted, but not orientational symmetry.

nature of the freezing transition in general 2D systems has been one of the central problems of statistical mechanics for nearly fifty years, and hard models have played an important role. Unlike in 3D, where HS undergo an unambiguous first-order fluid-crystal transition, thermal fluctuations are much stronger in 2D and prevent true long-range translational order. Instead, a crystal exhibits only quasi-long-range positional order, while orientational order can remain truly long-ranged. This immediately suggested that melting in 2D might belong to a different universality class.

Early computer simulations of hard discs (e.g. Alder and Wainwright in the 1960s) appeared to show a conventional first-order transition, analogous to 3D freezing, with coexistence between fluid and crystal phases, and for nearly two decades this remained the accepted picture. However, the situation changed drastically with the work of Kosterlitz et al. during the late 1970s: the KTHN theory.

This theory predicts that melting is driven by the unbinding of topological defects, rather than by ordinary nucleation as in a standard first-order transition. There are two continuous transitions: from crystal to hexatic, where dislocation pairs unbind, positional order changes from algebraic to short-ranged, but orientational order remains quasi-long-ranged; and from hexatic to isotropic fluid, where disclinations unbind and orientational order also becomes short-ranged. The intermediate hexatic phase is characterized by exponential decay of translational correlations and algebraic decay of bond-orientational correlations. This prediction was revolutionary because it introduced a completely new melting mechanism. In this case the defects are disclinations, isolated five- or seven-fold coordinated particles, and dislocations, consisting of bound pairs of disclinations (see Fig. 10).

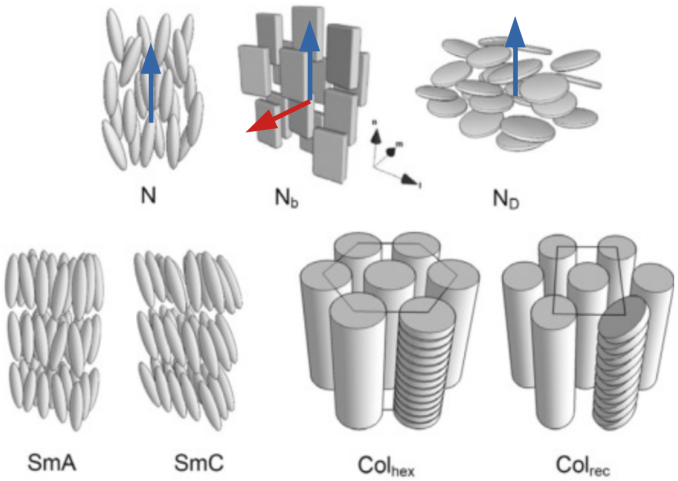


Figure 11: Different LC phases [7].

Nematic and other liquid-crystal phases in nonspherical hard models. We have discussed several anisotropic particle models before. These models are used in general to provide a theoretical basis for explaining the existence of orientational order in otherwise fluid or partially fluid systems: the so-called *liquid crystals* (LC).

Liquid crystals are phases of matter intermediate between the liquid and the crystal. They possess some degree of fluidity, while at the same exhibiting orientational order. Thus, they are anisotropic materials that flow like fluids (albeit in complicated ways due to the anisotropic properties) but have elasticity due to the broken orientational symmetry. The latter means that they possess elastic constants associated to changes in the local orientation of the particles and corresponding changes in the free energy.

Fig. 11 illustrates the simplest LC phases. First we have the *nematic* (N), where particles orient along a specific direction on average, while their centres of mass move freely (with typical short-range correlations). The average orientation is called the *director*, which can be described as a local vector field $\hat{\boldsymbol{n}}(\boldsymbol{r})$. A relaxed nematic, free from boundaries (which is an ideal case), will have $\hat{\boldsymbol{n}}(\boldsymbol{r}) = \textbf{const.}$ When $\nabla\hat{\boldsymbol{n}} \neq \boldsymbol{0}$ the free energy of the system increases because of the stiffness of the material to orientational gradients. We will conver this topic later in the course.

Orientational symmetry is thus broken in nematics. The nematic phase is typically obtained from the fully symmetric *isotropic* (where the system is disordered both in translations and rotations, and no symmetry is broken). Going to the isotropic to the nematic can usually be realised by lowering the temperature in systems with attractive interactions like elongated molecules. But in elongated colloidal particles, such as polymer particles, bacteria or viruses, the transition is driven by density, because interactions are closer to being hard and temperature plays no role. Depending on the anisotropy of the particle, we may have biaxial nematics (N_b) or discotic nematic (N_D). To exhibit nematic phases particles need to have a sufficiently high degree of anisotropy. For example, for rod-like particles, the critical value of length to breadth is ~ 4.5 [8].

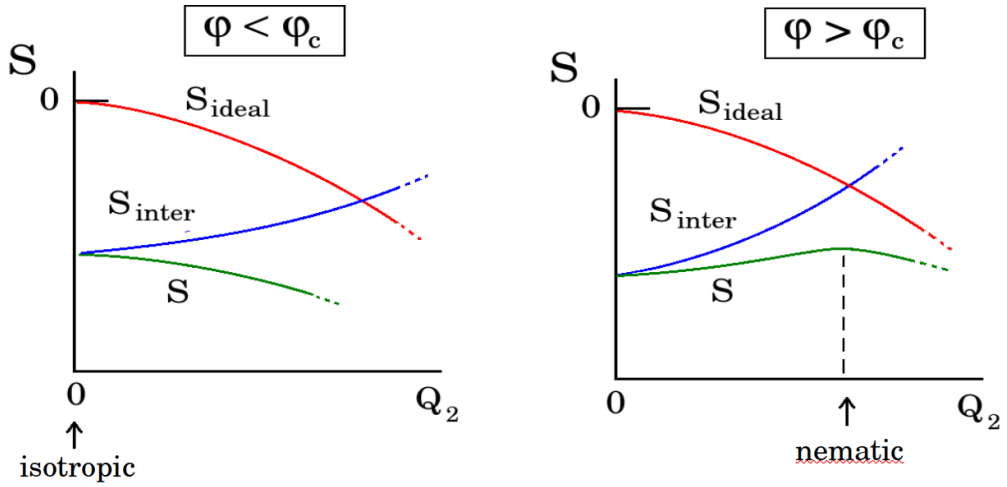


Figure 12: For low densities, the total energy of the system S is maximum when the nematic order parameter $Q_2 = 0$, i.e. the system is in the isotropic phase. This is because the ideal rotational entropy S_{ideal} wins over the interaction entropy S_{inter}. For high densities however, the interaction entropy dominates, resulting in a maximum of the total entropy at some value $Q_2 > 0$: a nematic phase is stabilized.

At first sight the stabilization of nematic phases in purely repulsive models is as puzzling as the

formation of the HS crystal phase. One would expect the tendency of neighbouring particles to remain parallel in the nematic phase to be caused by specific attractive interactions, mostly from van der Waals forces integrated over the surface of the particles. This is the mechanism behind the formation of liquid-crystal phases in molecular systems. However, entropy alone can explain nematic order without the need of attractive forces. We can write the entropy as the sum of two contributions:

$$S = S_{\text{ideal}} + S_{\text{inter}}, \tag{13}$$

where, in a system of anisotropic particles, $S_{\text{ideal}} = S_{\text{trans}} + S_{\text{orient}}$ has translational and orientational parts. The translation part does not play a role for nematics, although it will be important for liquid crystals exhibiting spatially ordered phases.

Hard models for anisotropic particles predict an isotropic-nematic transition as the density is increased when the particle anisotropy is sufficiently large. The reason lies in the entropy. This was predicted theoretically by Onsager [9] for hard rods, and later confirmed by computer simulation by Frenkel [10]. The critical aspect ratio beyond which a nematic phase is stabilised depends a bit on the model, but it is about 3-4. The mechanism behind the transition is again explained in terms of entropy, Fig. 12. The ideal rotational entropy S_{ideal} always decreases as the order parameter Q_2 increases, so that it always favours an isotropic phase ($Q_2 = 0$). However, the interaction entropy S_{inter} shows the opposite behaviour. For a packing fraction $\varphi < \varphi_c$ the rotational entropy wins, and the system remains disordered in the isotropic phase. However, if $\varphi > \varphi_c$, it is the interaction entropy which dominates, and a phase transition to the nematic phase occurs. Again the reason for this is that the interaction entropy is proportional to the logarithm of the volume (or area) available to the particles. This volume is maximised when the excluded volume is minimised, i.e. when the particles tend to be aligned along a common direction, as shown in Fig. 13.

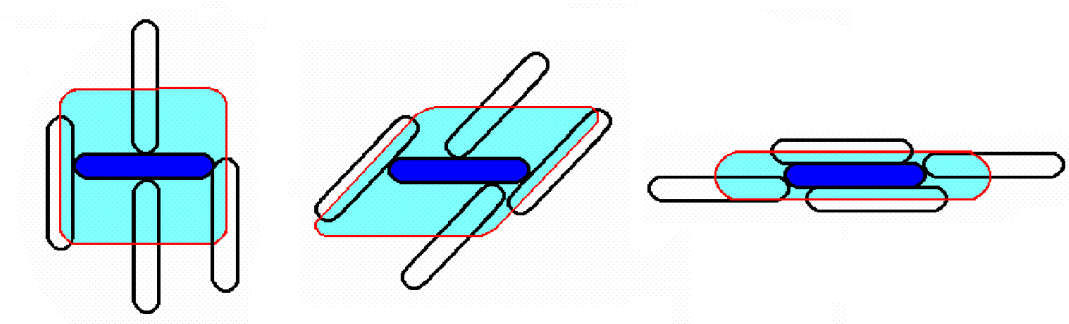


Figure 13: The excluded volume between two rods is minimised when the rods are aligned. This means that the volume available to the particles is increased, causing a maximum in the interaction entropy. This argument applies to two rods, but the concept can be extended to systems of many interacting rods.

2D nematics are also formed, but they are peculiar, again due to the low dimensionality and the importance of fluctuations beacuse of the reduced local binding of particles. For example, the angular correlation is not long-ranged, but quasi-long-ranged, as the translational order in 2D

crystals.

Particles can also form *smectic* phases, i.e. nematic phases where a density wave is developed along a particular direction. The system remains in a quasi-2D fluid state in the planes perpendicular to the ordering direction. So we may think of the smectic as a stacking configuration of quasi-2D layers of particles in a fluid state. When the ordering direction coincides with the direction of alignment we have the smectic-A type. Other smectic types may exist. Computer simulations have been conducted to study the formation of smectic phases is systems of hard particles.

Higher-order symmetries in polygonal hard particles. Polygons in 2D and polyhedra in 3D show interesting orientational properties and exhibit phases with orientational order, intermediate between the fluid and the crystal. Particularly interesting for the aims of this course are particles in 2D. Fig. 14 shows a sequence of polygonal particles with increased number of sides. These particles have been studied extensively (see e.g. [11]).

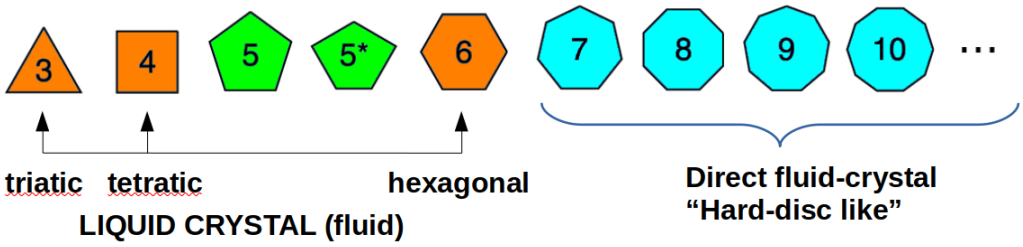


Figure 14: Series of polygonal particles. Polygons with less than $p = 7$ sides stabilise liquid-crystal phases of various symmetries.

It turns out that polygons with $p = 7$ sides or more behave just like hard discs, and undergo a direct transition from the fluid to the crystal. However, polygons with $p = 3-6$ sides can stabilize liquid-crystal phases. The symmetry of these phases are very dependent on the shape of the particles, but the most interesting aspect of these phases is that they are *highly-symmetric phases*, with mutiple equivalent directors. The orientational distribution function is symmetric with respect to rotations of less than π (the usual symmetry for a 2D nematic, or 2-atic phase). For example, equilateral triangles ($p = 3$) stabilize a triangular or 6-atic phase, with symmetry under rotations by 60°. Squares stabilize the so-calles *tetratic* phase (4-atic phase), with symmetry under 90°. All of these phases are more symmetric than the usual nematic.

1.8 Density-functional Theory: exactly solved hard-body model in 1D

Classical density-functional theory (DFT) provides a general framework for describing inhomogeneous fluids in thermal equilibrium [12]. Its fundamental variable is the one-body density distribution $\rho(\boldsymbol{r},\boldsymbol{\Omega})$, from which all equilibrium properties of the system can, in principle, be obtained. Here $\boldsymbol{r}$ is a position describing the particle's position, and $\boldsymbol{\Omega}$ a set of angles describing the particle orientation, so that

$$\rho(\boldsymbol{r},\boldsymbol{\Omega})d\boldsymbol{r}d\boldsymbol{\Omega} \tag{14}$$

gives the average number of particles within the differential volume $d\boldsymbol{r}$ centred at $\boldsymbol{r}$ and with an orientation within some solid angle sector $d\boldsymbol{\Omega}$ about $\boldsymbol{\Omega}$. Obviously the one-body density distribution saisfies

$$\int_V d\boldsymbol{r} \int d\boldsymbol{\Omega} \rho(\boldsymbol{r},\boldsymbol{\Omega}) d\boldsymbol{r} d\boldsymbol{\Omega} = N, \tag{15}$$

the total number of particles. V is the volume of the system.

The central quantity in DFT is the Helmholtz free-energy functional, $F[\rho]$, which is universal in the sense that it depends only on the intermolecular interactions and not on the external potential acting on the system. It is conveniently decomposed into an exactly known ideal-gas contribution and an excess part accounting for particle interactions,

$$F[\rho] = F_{\mathrm{id}}[\rho] + F_{\mathrm{ex}}[\rho], \tag{16}$$

where

$$F_{\mathrm{id}}[\rho] = kT \int_V d\boldsymbol{r} \int d\boldsymbol{\Omega} \rho(\boldsymbol{r},\boldsymbol{\Omega}) d\boldsymbol{r} d\boldsymbol{\Omega} \left\{ \log \left[\rho(\boldsymbol{r},\boldsymbol{\Omega}) \Lambda^3 \right] - 1 \right\}, \tag{17}$$

and $F_{\mathrm{ex}}[\rho]$ contains all the effects of intermolecular correlations. The construction of accurate approximations for $F_{\mathrm{ex}}[\rho]$ is the central problem of classical DFT.

For systems in the grand-canonical ensemble, where the temperature T, chemical potential μ, and external potential $V_{\mathrm{ext}}(\boldsymbol{r},\boldsymbol{\Omega})$ are prescribed, it is convenient to introduce the grand-potential functional,

$$\Omega[\rho] = F[\rho] + \int_V d\boldsymbol{r} \int d\boldsymbol{\Omega} \rho(\boldsymbol{r},\boldsymbol{\Omega}) \left[V_{\mathrm{ext}}(\boldsymbol{r},\boldsymbol{\Omega}) - \mu \right]. \tag{18}$$

The cornerstone of classical DFT is the variational principle established by Mermin and later formulated in its modern form by Evans: among all physically admissible density distributions, the equilibrium density minimizes the grand-potential functional. Thus, the equilibrium profile ρ_{eq} satisfies

$$\Omega[\rho_{\mathrm{eq}}] = \min_{\rho} \Omega[\rho] \tag{19}$$

or, equivalently, the Euler-Lagrange equation:

$$\frac{\delta F[\rho]}{\delta \rho} + V_{\mathrm{ext}}(\boldsymbol{r},\boldsymbol{\Omega}) = \mu. \tag{20}$$

Once a suitable approximation for the excess free-energy functional is available, this variational principle allows one to predict equilibrium density profiles, adsorption, interfaces, confinement effects, and phase transitions within a unified theoretical framework. The advantage of the density-functional formalism with respect to the standard procedure based on the partition function is that it is comparatively simpler to develop sensible approximations for the excess

free-energy functional.

2 Scaled-Particle Theory in 2D. Monte Carlo simulation

In this chapter we will focus on the derivation of some results which turn out to be crucial for the development of density-functionals. In the '80s of the last century a large effort was put into developing accurate DFT functionals. The idea was to use various techniques (gradient expansions, perturbation theory, weighted-density approximations, etc.) to obtain accurate functionals for some specific dimensionality, using bulk information (equation of state and direct correlation function of the fluid). However, these functionals, although very accurate in certain situations, failed completely when the system was severely confined along one or more directions, like in a fluid confined into a planar slit or a spherical cavity. The reason was that the functionals were based on two-particle correlations in the bulk, which are isotropic; however, in very anisotropic environments these approximations are very bad.

At the end of the '80s and the beginning of the '90s a completely new idea was proposed. Instead of focusing on two-particle correlations, it was shown to be much more fruitful to focus on one-particle geometry, much in the same way as the older Scaled-Particle Theory (SPT) was developed. The Fundamental-Measure Theory [2, 15] was born). It turned out that by incorporating the particle geometry through adequately defined weighting measures, giving the geometrically-based SPT theory for granted, a coherent and consistent scheme emerged for the density functionals. A central idea, related to the geometrical concepts, was also proposed: *dimensional consistency* or *dimensional crossover* must apply to the functionals, allowing to recover the functional in one dimensionality from the functional at a higher dimensionality. Playing with this concept, and extending the idea, it was proposed that dimensional consistenty can be used as a design principle for functionals, starting from the simplest one, at zero dimensionality ($D = 0$), and going up in dimensionality, thus obtaining very accurate functionals for more realistic situations. To explore these ideas we have to start by deriving the exact functionals at $D = 0$ and $D = 1$.

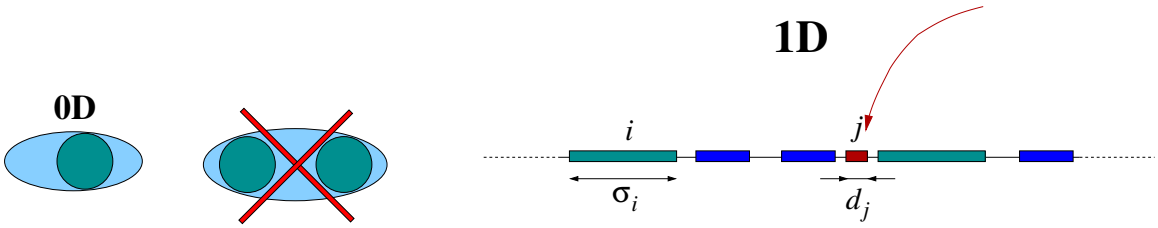


Figure 15: Left: Sketch of the 0D-cavity where only one particle entes inside. Right: A 1D hard-rod mixture of sizes σ_i ($i = 1, \ldots$,c) with c the number of components. An scaled particle of dimension d_j is inserted from outside.

The most simple model one can imagine consists on one particle inside a general cavity which is small enough that no more than one particle hold inside it (see Fig. 15). Calling η, with $0 \leq \eta \leq 1$, the particle occupation fraction, the probability of particle insertion inside the cavity is $P = 1 - \eta$. The work necessary to insert a particle inside the cavity is an alternative definition of the so called excess, over the ideal-gas part, of the chemical potential $\beta\mu^{(\mathrm{exc})}$, scaled with the inverse of the temperature $\beta = (k_B T)^{-1}$. The Boltzmann factor and the probability of particle insertion is the same magnitude: $e^{-\beta\mu^{(\mathrm{exc})}} = P = 1 - \eta$. Using the simple thermodynamic

equation that relates the excess part of the chemical potential with the derivative with respect to η of the excess, or interaction part, of the Helmholtz free-energy $\mu_{\rm exc} = F'_{\rm exc}(\eta)$, we obtain by integration, and considering the zeroth integration constant compatible with $F_{\rm exc}(0) = 0$, the following expression:

$$\Phi_{\rm 0D} \equiv \beta F_{\rm exc}(\eta) = \eta + (1-\eta)\ln(1-\eta)\,, \tag{21}$$

which we call the excess free-energy of the zeroth-dimensional cavity.

Following the same recipe but now in one dimension, $D = 1$, we consider a multicomponent fluid mixture of hard segments of lengths $\{\sigma_i\}_{i=1}^{c}$ (with c the number of components) that can not overlap. The probability to insert a new particle of dimension d_j in this one-dimensional fluid (see Fig. 15) when $d_j \to 0$ is

$$P_j = e^{-\beta\mu_j^{\rm (exc)}} = 1 - \sum_i \underbrace{\frac{N_i}{L}}_{\rho_i}(\sigma_i + d_j), \tag{22}$$

where we have defined ρ_i as the number density of species i and $\sigma_i + d_j$ is the excluded, to the inserted particle, length due to the presence of particle i. In the other macroscopic limit, when $d_j \to \infty$, the work to insert the particle is equal to the work, against the fluid pressure, to open a macroscopic cavity of dimension d_j, i.e. $\mu_j^{\rm (exc)} = p d_j$. Thus, taking both limits into account and substituting $d_j = \sigma_j$ (the dimension of one of the species) we obtain the expression for the excess part of the chemical potential

$$\beta\mu_j^{\rm (exc)} = -\ln(1-\eta) + p\sigma_j, \tag{23}$$

that interpolates between small and large particle dimensions. $\eta = \sum_i \rho_i\sigma_i$ is the total packing fraction of the mixture. Resorting to the exact thermodynamic equation that relates the fluid pressure with the excess part of the chemical potential:

$$\beta p = \sum_i \rho_i \left(1 + \beta\mu_i^{\rm (exc)}\right) - \Phi_{\rm 1D}, \quad \beta\mu_i^{\rm (exc)} = \frac{\partial\Phi_{\rm 1D}}{\partial\rho_i}, \tag{24}$$

we obtain the excess part of the free energy per unit of length of the one-dimensional uniform fluid

$$\Phi_{\rm 1D} = -\rho\ln(1-\eta), \quad \rho = \sum_i \rho_i, \tag{25}$$

with ρ the total number density of the fluid, i.e. $\rho = N/L$, with N and L the total number of particles and the system length respectively. This expression coincides with the exact expression obtained from the transfer-matrix formalism, which constitutes a recipe to obtain the partition function of the system, and from it the free-energy of the fluid mixture of hard rods. This recipe to obtain the free-energy of a general mixture by interpolating the work necessary to open a cavity of dimensions that range from vanishing small to that of macroscopic dimensions inside the fluid is called the scaled particle theory (SPT) [16]. It is nice that despite this formalism

is not based on exact calculations the result for zeroth and one dimension coincides with those obtained from the exact partition function calculations. The extension of the SPT to higher dimensions (2D and 3D) unfortunately does not produce an exact result. However being an approximation it has been extensively applied to study the phase behavior of uniform fluids of general hard particles with geometries ranging from disks, rectangles, ellipses, triangles, to more exotic shapes like kites. As the SPT for two-dimensional mixtures of general hard particles constitutes one of the cornerstone of the present course, we will formulate it a bit later.

But before that we will obtain the exact expression for the free-energy density-functional of the non-uniform fluid mixture of hard segments in 1D. This time the number density of species i is not uniform, it depends on the spatial x-coordinate $\rho_i(x)$. Taking into account the mathematical structure of $\Phi_{\rm 1D}$ from Eq. (25) we now define two weighting densities $n_0(x)$ and $n_1(x)$, such that they fulfills the uniform limit conditions $n_0(x) \to \rho$, and $n_1(x) \to \eta$ and are calculated by averaging or convoluting the density profile of species i, $\rho_i(x)$, over a region of dimensions of one particle-length σ_i, weighted with certain functions $\omega_i^{(0)}(x)$ and $\omega_i^{(1)}(x)$, selected in such a way to correctly capture the particle correlations at least at the low density limit. Then we need to take the sum over species of these convolutions. Thus we propose:

$$n_\alpha(x) = \sum_i \int dx' \rho_i(x') \omega_i^{(\alpha)}(x - x'), \quad \alpha = 0,1, \tag{26}$$

and the excess part of the Helmholtz free-energy density is now

$$\Phi_{\rm 1D}(x) = -n_0(x) \ln\left(1 - n_1(x)\right), \tag{27}$$

which integral over the spatial coordinate give us the excess part of the Helmholtz density functional:

$$\beta \mathcal{F}_{\rm exc}[\{\rho_i\}] = \int dx \Phi_{\rm 1D}(x). \tag{28}$$

The low density limit of (28) is exactly known as the Onsager approach [9] which involve a double integral of the Mayer or Heaviside function of the excluded length support, $(\sigma_i + \sigma_j)/2$, between the pair of rods ij, weighted with the density profiles $\rho_i(x)$ and $\rho_j(x')$, and summing over all the pairs:

$$\beta \mathcal{F}_{\rm exc}[\{\rho_i\}] \sim \frac{1}{2} \sum_{i,j} \int dx \int dx' \rho_i(x) \rho_j(x') \Theta\left(\frac{\sigma_i + \sigma_j}{2} - |x - x'|\right), \tag{29}$$

with $\Theta(x)$ the Heaviside function. Thus, the first term in the expansion of the second functional derivative of (28) should coincide with that of Eq. (29) giving us the relation

$$\Theta\left(\frac{\sigma_i + \sigma_j}{2} - |x|\right) = \int dx' \left(\omega_i^{(0)}(x') \omega_j^{(1)}(x - x') + \omega_i^{(1)}(x') \omega_j^{(0)}(x - x')\right), \tag{30}$$

which allows us to find the weighting functions:

$$\omega_i^{(0)}(x) = \frac{1}{2}\delta\left(\frac{\sigma_i}{2} - |x|\right), \quad \omega_i^{(1)}(x) = \Theta\left(\frac{\sigma_i}{2} - |x|\right). \tag{31}$$

Thus the weighted densities are

$$n_0(x) = \frac{1}{2}\sum_i \left[\rho_i\left(x - \frac{\sigma_i}{2}\right) + \rho_i\left(x + \frac{\sigma_i}{2}\right)\right], \tag{32}$$

$$n_1(x) = \sum_i \int_{x-\sigma_i/2}^{x+\sigma_i/2} dx' \rho_i(x'). \tag{33}$$

An this, taking into account Eq. (27), completely define the excess Helmholtz density functional (28). Surprisingly this expression for the excess part of the Helmholtz density functional for the fluid mixture of hard rods in 1D coincides with the exact one as it was shown in Ref. [13].

The ideal-gas (non-interacting) part of the Helmholtz free-energy of the fluid mixture is known exactly as

$$\beta\mathcal{F}_{\rm id}[\{\rho_i\}] = \sum_i \int dx \rho_i(x)\left[\ln\left(\rho_i(x)\mathcal{A}_i\right) - 1\right], \tag{34}$$

with $\mathcal{A}_i$ the thermal area of species i. Thus the Legendre transform of the total free-energy functional, $\mathcal{F}[\{\rho_i\}] = \mathcal{F}_{\rm id}[\{\rho_i\}] + \mathcal{F}[\{\rho_i\}]$, the sum of the ideal and the excess part, with respect to the number of particles define the grand-canonical density functional:

$$\Omega[\{\rho_i\}] = \mathcal{F}[\{\rho_i\}] - \sum_i \mu_i \int dx \rho_i(x'), \tag{35}$$

with μ_i the chemical potential of species i. Finally if the fluid is under the effect of an external potential $v_i^{(\rm ext)}(x)$ acting on each species i the total grand-potential is

$$\Omega[\{\rho_i\}] = \mathcal{F}[\{\rho_i\}] + \sum_i \int dx \rho_i(x)\left(v_i^{(\rm ext)}(x) - \mu_i\right). \tag{36}$$

The key idea of the density functional theory is that the density functional minimization of (36) gives us the equilibrium density profiles $\{\rho_i(x)\}$ under the fixed values of chemical potentials $\{\mu_i\}$:

$$\frac{\delta\Omega[\{\rho_i\}]}{\delta\rho_i} = 0 \Rightarrow \ln\left(\rho_i(x)\mathcal{A}_i\right) - c_i^{(1)}(x) + v_i^{(\rm ext)}(x) - \mu_i = 0, \tag{37}$$

where the one-body correlation functions of species i is defined as

$$-c_i^{(1)}(x) = \frac{\delta\mathcal{F}_{\rm exc}[\{\rho_i\}]}{\delta\rho_i(x)} = \sum_\alpha \int dx' \frac{\partial\Phi_{\rm 1D}}{\partial n_\alpha(x)}\omega_i^{(\alpha)}(x - x'). \tag{38}$$

2.1 A working example: confined hard rods in 1D

Suppose that a one component fluid is inside a slit of width H which confines the fluid between two hard walls positioned at $x = 0$ and $x = H$, i.e. the external potential acting on a hard rod of dimension σ is

$$v_i^{(\mathrm{ext})}(x) = \begin{cases} \infty, & 0 \leq x < \frac{\sigma}{2} \text{ or } H - \frac{\sigma}{2} < x \leq H, \\ 0, & \frac{\sigma}{2} \leq x \leq H - \frac{\sigma}{2} \end{cases} \tag{39}$$

This in turn implies that the density profile is different from zero only for $x \in \left[\frac{\sigma}{2},H - \frac{\sigma}{2}\right]$. Thus inverting the Eq. (37) particularized for the one component fluid we obtain

$$\rho(x) = e^{\beta\mu + c(x)}, \text{ for } x \in \left[\frac{\sigma}{2},H - \frac{\sigma}{2}\right], \text{ otherwise } \rho(x) = 0, \tag{40}$$

$$-c(x) = -\frac{1}{2}\ln\left[\left(1 - n_1\left(x - \sigma/2\right)\right)\left(1 - n_1(x + \sigma/2)\right)\right] + \int_{x-\sigma/2}^{x+\sigma/2} dx' \frac{n_0(x')}{1 - n_1(x')}, \tag{41}$$

$$n_0(x) = \frac{1}{2}\left[\rho\left(x - \frac{\sigma}{2}\right) + \rho\left(x + \frac{\sigma}{2}\right)\right], \, n_1(x) = \int_{x-\sigma/2}^{x+\sigma/2} dx' \rho(x') \tag{42}$$

Fixing the chemical potential $\beta\mu$ we can solve Eq. (40) to find the equilibrium density profile $\rho_{\mathrm{eq}}(x)$. To that purpose a simple numerical recipe to solve it is to use a mixed fixed point algorithm, i.e.

$$\rho^{(k+1)}(x_i) = (1 - r)\rho^{(k)}(x_i) + re^{\beta\mu + c_k(x_i)}\Theta\left(\frac{H - \sigma}{2} - \left|x_i - \frac{H}{2}\right|\right), \tag{43}$$

with $\Theta(x)$ the Heaviside step function, where $0 \leq r \leq 1$ is the mixing parameter, and $c_k(x_i)$ is the function $c(x)$ defined by Eq. (41) evaluated at the density profile in the kth iterative step $\{\rho_k(x_i)\}$. The iteration procedure should stop when a given tolerance,

$$\epsilon \equiv \sum_{i=1}^{N} |\rho^{(k+1)}(x_i) - \rho^{(k)}(x_i)| \tag{44}$$

is reached. Note that we need to discretize the total length $[0,H]$ in a set of grid-points,

$$\left\{x_i = \frac{iH}{N}\right\}, \quad i = 0,1,\ldots,N. \tag{45}$$

2.2 Dimensional crossover

An important property that any exact density-functional (in particular its excess part) should fulfill is the dimensional crossover criterion. Suppose that the particles of a D-dimensional fluid is constrained in such a way that its density profile is given by

$$\rho_{\mathrm{D}}(x_1,x_2,\ldots,x_{\mathrm{D}}) = \rho_{\mathrm{D}-1}(x_1,x_2,\ldots,x_{\mathrm{D}-1})\delta(x_{\mathrm{D}}), \tag{46}$$

with $\delta(x)$ de Dirac-delta function, i.e. the particles are confined at the hyperplane $x_{\mathrm{D}} = 0$. Then any exact D-dimensional density functional, evaluated at this constrained density profile, should

fulfills the property:

$$\mathcal{F}_{\rm ex}^{(\rm D)}[\rho_d] = \mathcal{F}_{\rm ex}^{(\rm D-1)}[\rho_{\rm D-1}], \tag{47}$$

where $\mathcal{F}_{\rm ex}^{(\rm D-1)}$ is the exact density functional of the $d-1$-dimensional fluid.

For $d > 1$ $\mathcal{F}_{\rm ex}[\rho]$ is no more an exact density functional, only it can be approximated. But we can require for it the dimensional cross-over property with the conviction that this requirement will produce a well- performing density functional in the description of a highly confined fluid.

Implementing the dimensional cross-over from $d = 1$ to $d = 0$, i.e. inserting the constrained density profile $\rho_1(x) = \eta\delta(x)$ into Eq. (28) for the excess part of the hard-rods density functional, we obtain

$$\mathcal{F}_{\rm exc}[\rho_1] = \Phi_{\rm 0D}(\eta), \tag{48}$$

which is the excess part density-functional of the zeroth dimensional cavity (21), as should be.

If we now define the function

$$\tilde{\Phi}_{\rm 0D} \equiv \int dx \Phi_{\rm 0D}(\eta(x)) = \int dx \left[\eta(x) + (1-\eta(x))\ln(1-\eta(x))\right], \tag{49}$$

where we define the local packing fraction as

$$\eta(x) = \rho_1 * \omega^{(1)}(x) = \int dx' \rho(x')\omega^{(1)}(x-x') = \int_{x-\sigma/2}^{x+\sigma/2} dx' \rho_1(x'), \quad \omega^{(1)}(x) = \Theta\left(\frac{\sigma}{2} - |x|\right), \tag{50}$$

applying to $\tilde{\Phi}_{\rm 0D}$ the and differential operator

$$\mathcal{D} \equiv \frac{\partial}{\partial\sigma}, \tag{51}$$

we obtain the 1-dimensional density functional from the 0-dimensional one:

$$\mathcal{F}_{\rm exc}[\rho_1] = \mathcal{D}\tilde{\Phi}_{\rm 0D}, \tag{52}$$

which is a direct consequence of the dimensional crossover property.

This interesting result in turn implies that we can generate a density functional also for a fluid of parallel hard squares applying the same procedure [14]:

(i) First we define the modified 0D DF and the two-dimensional local packing fraction:

$$\tilde{\Phi}_{\rm 0D} = \int dx \int dy \Phi_{0D}(\eta(x,y)), \tag{53}$$

$$\eta(x,y) = \int dx \int dy \rho(x,y)\omega^{(2)}(x-x',y-y'), \tag{54}$$

$$\omega^{(2)}(x,y) = \Theta\left(\frac{\sigma^{(x)}}{2} - |x|\right)\Theta\left(\frac{\sigma^{(y)}}{2} - |y|\right), \tag{55}$$

Let us define the differential operator

$$\mathcal{D} = \frac{\partial}{\partial \sigma^{(y)}} \frac{\partial}{\partial \sigma^{(x)}}. \tag{56}$$

Applying to $\tilde{\Phi}_{0\mathrm{D}}$ this differential operator and setting $\sigma^{(x)} = \sigma^{(y)} = \sigma$, we obtain the DF for a two-dimensional fluid of parallel hard squares:

$$\beta \mathcal{F}_{\mathrm{exc}}[\rho] = \int d\boldsymbol{r} \Phi_{2\mathrm{D}}(\boldsymbol{r}), \tag{57}$$

$$\Phi_{2\mathrm{D}}(\boldsymbol{r}) = -n_0(\boldsymbol{r}]) \ln(1 - n_2(\boldsymbol{r})) + \frac{n_{1x}(\boldsymbol{r}) n_{1y}(\boldsymbol{r})}{1 - n_2(\boldsymbol{r})}, \quad n_\alpha(\boldsymbol{r}) = \rho * \omega^{(\alpha)}(\boldsymbol{r}), \tag{58}$$

$$\omega^{(0)}(\boldsymbol{r}) = \frac{1}{4} \delta\left(\frac{\sigma}{2} - |x|\right) \delta\left(\frac{\sigma}{2} - |y|\right), \quad \omega^{(2)}(\boldsymbol{r}) = \Theta\left(\frac{\sigma}{2} - |x|\right) \Theta\left(\frac{\sigma}{2} - |y|\right), \tag{59}$$

$$\omega^{(1x)}(\boldsymbol{r}) = \frac{1}{2} \Theta\left(\frac{\sigma}{2} - |x|\right) \delta\left(\frac{\sigma}{2} - |y|\right), \quad \omega^{(1y)}(\boldsymbol{r}) = \frac{1}{2} \delta\left(\frac{\sigma}{2} - |x|\right) \Theta\left(\frac{\sigma}{2} - |y|\right). \tag{60}$$

Note that $n_2(x,y) = \eta(x,y)$. This density functional for parallel hard squares constitutes one example of the Fundamental-Measure Density Functionals, with the first one originally derived for a mixture of hard spheres by Rosenfeld [2] and a later version of it (fulfilling the dimensional crossover property) was successfully applied to the study of freezing of hard spheres [15]. The name comes from the integrals of the weigthed functions, $W_\alpha \equiv \int d\boldsymbol{r} \omega^{(\alpha)}(\boldsymbol{r})$, which produce the fundamental measures of a single particle: $W_0 = 1$ (its Euler characteristic), $W_2 = \sigma^2$ (the particle area), $W_{1x} = W_{1y} = \sigma$ (the particle edge-lengths along x and y respectively).

To evaluate the performance of the density functional (57) we calculate the equation of state (pressure vs. packing fraction), where the fluid pressure from the present theory can be computed from

$$\beta p = A_{\mathrm{cell}}^{-1} \int_{A_{\mathrm{cell}}} d\boldsymbol{r} \frac{\partial \Phi_{2\mathrm{D}}}{\partial n_3(\boldsymbol{r})} = A_{\mathrm{cell}}^{-1} \int_{A_{\mathrm{cell}}} d\boldsymbol{r} \left\{ \frac{n_0(\boldsymbol{r})}{1 - n_2(\boldsymbol{r})} + \frac{n_{1x}(\boldsymbol{r}) n_{1y}(\boldsymbol{r})}{(1 - n_2(\boldsymbol{r}))^2} \right\}, \tag{61}$$

where $A_{\mathrm{cell}} = [0,d] \times [0,d]$ is the unit cell of the simple square lattice with d its periodicity, in case of an equilibrium crystalline phase, or simply $A_{\mathrm{cell}} = d$ the periodicity along a single spatial variable x, in case of an equilibrium columnar phase, where the centers of mass of the squares are positioned along columns (without spatial ordering in each column) separated by a period d along x. Note that the magnitude d should be calculated from the minimization of the total free-energy with respect to it. In case the density profile is uniform, all the weighted densities, n_α, are constants and we don't need to perform the integration over the spatial variables $\boldsymbol{r} = (x,y)$ to calculate the pressure of the uniform fluid. The equation of state (61) as a function of the mean packing fraction $\eta = A_{\mathrm{cell}}^{-1} \int_{A_{\mathrm{cell}}} \rho(\boldsymbol{r}) \sigma^2$ is plotted in Fig. 16 (solid and dotted lines) together with Molecular Dynamics (MD) simulation results (solid circles). As we can see the overall performance of the theory when compared with MD simulations is very good. The theory predicts a uniform fluid-columnar phase transition at $\eta \approx 0.52$ and a columnar-crystal transition at $\eta \approx 0.78$ while simulations predicts the freezing transition from the uniform fluid at 0.8. The

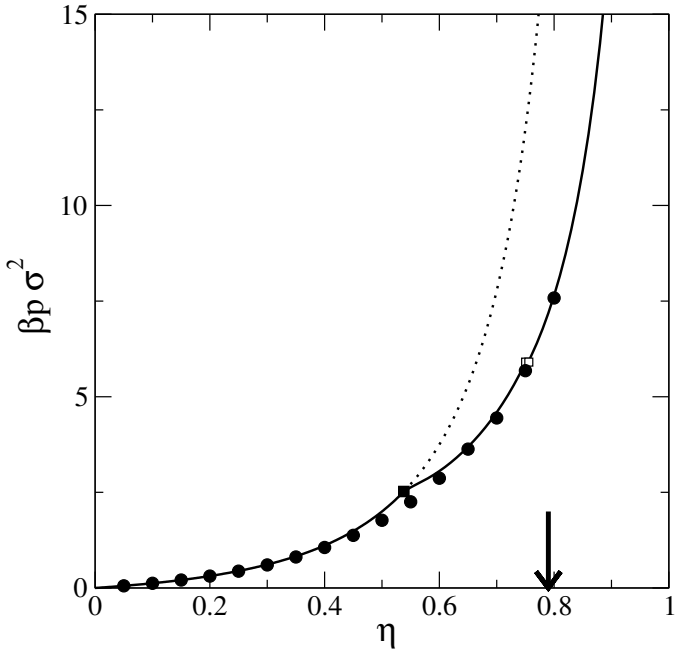


Figure 16: The equation of state (pressure vs. mean packing fraction) of a fluid of parallel hard squares. The results from the fundamental measure theory are plotted with solid line for the stable phases and dotted line for the metastable one (the uniform fluid at high η). The MD simulation results are indicated with solid circles. The solid square indicates the uniform fluid-columnar phase second order transition while the open squares indicates the columnar-crystal first order transition. The arrow indicates the packing fraction at the freezing transition given from MD simulations.

crystalline branch of the equation of state from the theory and MD simulations perfectly agree, something that we already expect because the Fundamental Measure Theory is constructed from the dimensional cross-over criterion and, consequently, should accurately describe highly inhomogeneous density profiles consisting on periodically spaced sharp peaks.

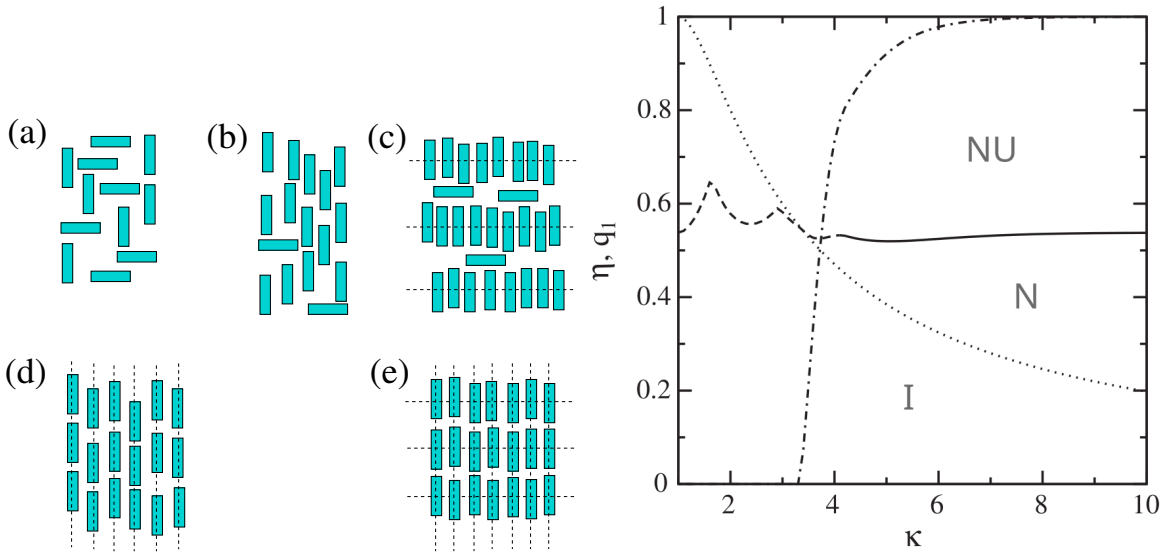


Figure 17: Left: Sketches of different phases of HR in the restricted orientations approximation (Zwanzig model). From low to high packing fractions we find the I (a), N (b), smectic (c) or columnar (d), and orientationally ordered crystal (e) phases. Right: The phase diagram in the packing fraction, η, aspect ratio $\kappa = L/\sigma$ plane, obtained from the Zwanzig model. Dotted line: I-N second order transition, solid and dashed lines: bifurcations from N or I phases to nonuniform phases (NU) such as the smectic (above the solid line) and columnar or plastic solid (above the dashed line). Dotted-dashed line: uniaxial order parameter q_1 along the N-NU spinodal.

2.3 Density functional for the 2D Zwanzig model

We can take advantage of the dimensional cross-over criterion to obtain a DF for the so called Zwanzig model of hard rectangles. Consider that the fluid is composed now of rectangles of length L and width σ ($L \geq \sigma$) with the main particle axes (those parallel to L) oriented parallel to one of Cartesian axis, x or y, of the fixed reference frame, i.e. HR can only rotate $\pm\frac{\pi}{2}$ instead to freely rotate. This constitutes an approximate model for a two-dimensional liquid crystal fluid as it can describe both the orientational disordered I fluid and the uniaxial N phase. But what is more important the model can be used also to study the relative stability of nonuniform phases, such as the smectic, plastic solid (a crystal without orientational degrees of freedoms) and the crystal phases.

We first introduce the two-dimensional tensor, $\sigma_\nu^{(\tau)}$, with $\tau,\nu = \{x,y,z\}$, which define the particle edge-length dimension along the Cartesian axis τ of the species with its main axis parallel to ν. Thus we have two species with their density profiles labeled as $\rho_\nu(\boldsymbol{r})$ ($\nu = \{x,y\}$). The expression for the tensor is

$$\sigma_\nu^{(\tau)} = \sigma + (L - \sigma)\,\delta_{\tau\nu}, \tag{62}$$

with $\delta_{\tau\nu}$ the Kronecker delta. Now can define the 0D modified free energy of the 0-dimensional cavity, identical to the expression (53), except that the total two-dimensional packing fraction is now

$$\eta(\boldsymbol{r}) = \sum_{\nu=x,y} \int d\boldsymbol{r}' \rho_\nu(\boldsymbol{r}) \omega_\nu^{(2)}(\boldsymbol{r}-\boldsymbol{r}'), \tag{63}$$

$$\omega_\nu^{(2)}(\boldsymbol{r}) = \prod_{\tau=x,y} \Theta\left(\frac{\sigma_\nu^{(\tau)}}{2} - |\nu|\right). \tag{64}$$

Defining a new differential operator

$$\mathcal{D} = \prod_\tau \left(\sum_\nu \frac{\partial}{\partial \sigma_\nu^{(\tau)}}\right), \tag{65}$$

and applying it to $\tilde{\Phi}_{0D}$ we obtain the excess part of the free-energy density for the Zwanzig model Φ_{2D} with the same functional structure (58), except that the weighted densities are now the following sums over species of convolutions between the density profiles and the weighting functions:

$$n_\alpha(\boldsymbol{r}) = \sum_\nu \int d\boldsymbol{r}' \rho_\nu(\boldsymbol{r}') \omega_\nu^{(\alpha)}(\boldsymbol{r}-\boldsymbol{r}'), \tag{66}$$

$$\omega_\nu^{(0)}(\boldsymbol{r}) = \frac{1}{4}\prod_\tau \delta\left(\frac{\sigma_\nu^{(\tau)}}{2} - |\nu|\right), \quad \omega_\nu^{(1\alpha)}(\boldsymbol{r}) = \frac{1}{2}\Theta\left(\frac{\sigma_\nu^{(\alpha)}}{2} - |\alpha|\right)\delta\left(\frac{\sigma_\nu^{(\gamma)}}{2} - |\gamma|\right), \ \gamma \neq \alpha \tag{67}$$

And this completely defines the density functional for the Zwanzig model. The sketch of the phases that the present model can stabilize is shown in Fig. 17. Defining the uniaxial nematic order parameter

$$q_1 = \frac{\rho_x - \rho_y}{\rho_x + \rho_y}, \tag{68}$$

with $q_1 \in [0,1]$, where we suppose that the nematic director is along the x axis, we can quantify the degree of orientational ordering of hard rectangles. For high enough densities and moderate aspect ratios $\kappa = L/\sigma$ the N phase (with $q_1 \neq 0$) is stable or metastable. We can find the value η^* such that $\lim_{\eta\to\eta^*} q_1(\eta) = 0$. This value, η^*, defines the I-N bifurcation as it is shown with dotted line in Fig. 17 for certain range of aspect ratios. This I-N bifurcation curve (dotted line) separates the regions of stability of I and N phases. However when η is relatively high the N phase is metastable with respect to nonuniform phases such as smectic phase (Sm) (above the solid line in Fig. 17) where the centers of mass of rectangles are periodically positioned along layers separated by a period d and with their main axes perpendicular to the layers. Also, the N or I phases can bifurcate to the columnar phase (C), again with a layered structure but now the main axes are parallel to the layers, or to the plastic solid (PS) (above the dashed curve), where the centers of mass are positioned at the nodes of a simple square lattice without orientational ordering of particles.

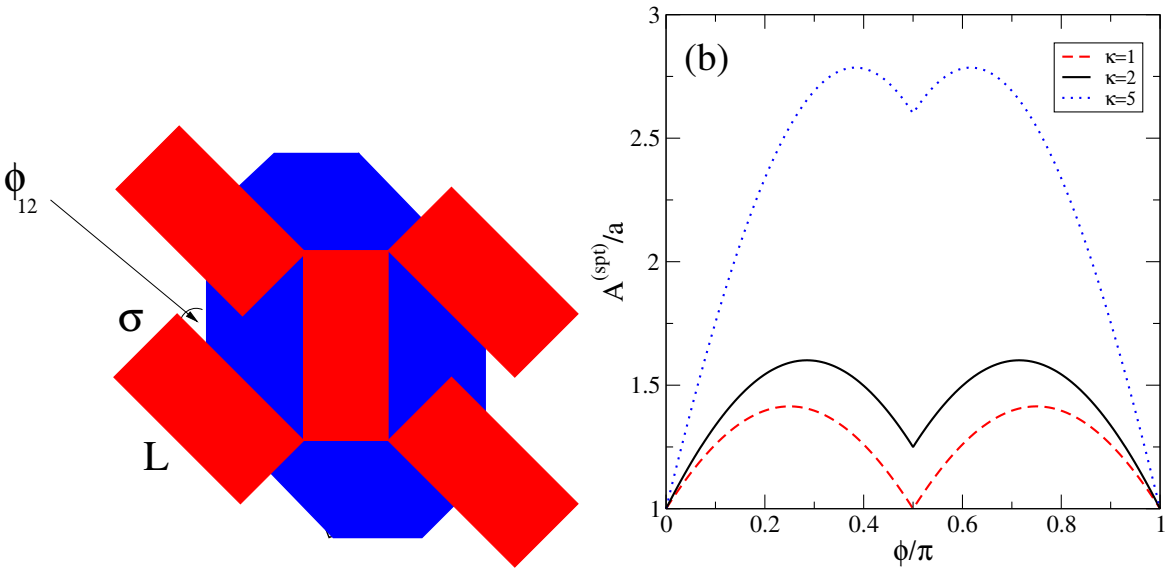


Figure 18: (a): Sketch of the excluded area (in blue) of two rectangles of length L and width σ with ϕ_{12} being the relative angle between main particle axes (those parallel to the sides of length L). (b): SPT-areas $A^{(\mathrm{spt})}(\phi)$ for $\kappa = L/\sigma = 1$ (hard squares), 2 and 5.

2.4 Scaled particle theory

The uniform limit of $\beta\mathcal{F}_{\mathrm{exc}}/A$ from Eq. (57) (with A the total area of the system), i.e the density profile being uniform $\rho(x,y) = \rho$, gives us

$$\Phi_{2\mathrm{D}} = -\rho\ln(1-\eta) + \frac{(\rho\sigma)^2}{1-\eta}, \tag{69}$$

with η the uniform limit of the local packing fraction $\eta = \rho a$, being $a = \sigma^2$ the particle area. This expression for the free-energy density can be written as a function of the excluded area between two squares, $A^{\mathrm{excl}} = 4\sigma^2$, as

$$\Phi_{2\mathrm{D}} = -\rho\ln(1-\eta) + \frac{1}{2}\frac{\rho^2\left(A^{(\mathrm{excl})} - 2a\right)}{1-\eta}, \tag{70}$$

The excluded area, considering that hard particles cannot overlap, is defined as the region of the space where a particle can not enter from the presence of the other one. For the case of parallel hard squares the excluded area is just a square with twice the particle dimensions. The formal expression (70) is justified by its low density limit $\rho \to 0$:

$$\Phi_{2\mathrm{D}} \sim \frac{1}{2}\rho^2 A^{(\mathrm{excl})}, \tag{71}$$

which is called the Onsager approximation and constitutes its exact limit.

The nice property of the form of $\Phi_{2\mathrm{D}}$ given from Eq. (70), known as the scaled particle theory (SPT) expression for the free-energy density, is that it can be extended to any particle geometry, for example to rectangles, triangles, etc. These particles, being anisotropic, have orientational degrees of freedoms, i.e. the number density, $\rho(\phi)$, depends on the angle ϕ that the main particle axis form with respect to a Cartesian axis of a fixed reference frame. Thus, considering a uniform

fluid with particles having orientational degrees of freedoms, the expression (70) can be extended to (withing the mark of the SPT), to

$$\Phi_{2D} = -\rho \ln(1-\eta) + \frac{\langle\langle A^{(spt)}\rangle\rangle}{1-\eta}, \tag{72}$$

where the so defined spt-area

$$A^{(spt)}(\phi_{12}) = \frac{1}{2}\left(A^{(excl)}(\phi_{12}) - 2a\right), \tag{73}$$

depends on the relative angle $\phi_{12} = \phi_1 - \phi_2$ between the main particle axes of particles 1 and 2. Note that in Eq. (72) enters the double angular average of the function $A^{(spt)}(\phi_{12})$ with respect to the number densities $\rho(\phi_1)$ and $\rho(\phi_2)$:

$$\langle\langle A^{(spt)}\rangle\rangle \equiv \int_0^{2\pi} d\phi_1 \int_0^{2\pi} d\phi_2 \rho(\phi_1)\rho(\phi_2) A^{(spt)}(\phi_{12}). \tag{74}$$

Note that, from the number density, $\rho(\phi) = \rho h(\phi)$, we can define the orientational distribution function, $h(\phi)$, as the probability density of particle being oriented with the angle ϕ with respect to a Cartesian axis of a fixed reference frame. Obviously this function is normalized: $\int_0^{2\pi} d\phi h(\phi) = 1$.

2.5 Fluid of hard rectangles (HR)

As a first example we give below the expression for the spt-area of rectangular particles with major and minor edge-lengths being L and σ respectively

$$A^{(spt)}(\phi) = \frac{\left(L^2+\sigma^2\right)}{2}|\sin\phi| + L\sigma|\cos\phi|. \tag{75}$$

We show in Fig. 18 (a) the excluded area between two rectangles and in panel (b) the function $A^{(spt)}(\phi)$ in the interval [0,π] for aspect ratios of particles $\kappa = L/\sigma = 1$ (hard squares), 2 and 5. For $\phi \in [\pi,2\pi]$ this function fulfills the symmetry $A^{(spt)}(\phi) = A^{(spt)}(\phi - \pi)$, which in turn is the result from the head-tail symmetry of the particle (the rectangle is invariant under rotation of π). Note the three local minima of this function at $\left\{0,\frac{\pi}{2},\pi\right\}$, with 0 and π being the same orientational state of the pair of particles, due to the head-tail symmetry. While $\{0,\pi\}$ are the absolute minima, which in turn implies that parallel particle configuration minimizes the excluded area, there exists a local minima at $\pi/2$, so the perpendicular configuration of particles locally minimizes the excluded area and consequently also locally minimizes the excess part of the free-energy density. However for $\kappa = 2$ the difference between the local and absolute minima is much smaller than that for $\kappa = 5$, something that affect, as we will see below the symmetry of the stable orientationaly ordered phase.

The exact ideal part of the free-energy density is

$$\Phi_{2D}^{(id)} = \int_0^{2\pi} d\phi \rho(\phi) \left[\ln\left(\rho(\phi)\mathcal{A}\right) - 1\right], \tag{76}$$

with $\mathcal{A}$ the thermal area which we drop as it will not affect the calculations necessary to produce the phase diagram. Minimizing the total free-energy $\Phi_{\rm 2D}^{\rm (tot)} = \Phi_{\rm 2D}^{\rm (id)} + \Phi_{\rm 2D}$ with respect to $\rho(\phi)$ and using the constraint $\int_0^{2\pi} d\phi h(\phi) = 1$ we obtain a non-linear integral equation for the function $h(\phi)$:

$$h(\phi) = T(\rho) e^{-\frac{2\rho}{1-\eta}\int_0^{2\pi} d\phi' h(\phi') A^{\rm (sp)}(\phi-\phi')}, \tag{77}$$

$$T(\rho)^{-1} \equiv \int_0^{2\pi} d\phi e^{-\frac{2\rho}{1-\eta}\int_0^{2\pi} d\phi' h(\phi') A^{\rm (spt)}(\phi-\phi')}. \tag{78}$$

Eqn. (77) should be solved to find the equilibrium orientational distribution function $h_{\rm eq}(\phi)$ for a fixed value of the number density ρ. An efficient method to numerically perform the calculations is to use Gauss-Legendre quadrature to estimate the angular integrals, selecting the set of nodes, $\{\phi_j\}$, and weights $\{t_j\}$ ($j = 1, \ldots, n$) corresponding to this quadrature and use the approximation $\int_0^{2\pi} d\phi f(\phi) = \int_{-\pi}^{\pi} d\phi f(\phi) = \pi \int_{-1}^{1} d\phi f(\pi\phi) \approx \pi \sum_{j=1}^{n} t_j f(\pi\phi_j)$. Then the Eq. (77) can be solved iteratively using the mixed fixed point algorithm: $h_k(\phi_j) = r h_{k-1}(\phi_j) + (1-r)\mathcal{K}[\{h_k(\phi_j)\}]$, where $\mathcal{K}$ is the right hand side of Eq. (77) evaluated at the orientational distribution function at the $k-1$ iteration step.

The ideal part of the free-energy, $\Phi_{\rm 2D}^{\rm (id)}$, has its absolute minimum value when the particle axes are randomly oriented (i.e. for the uniform distribution $h(\phi) = (2\pi)^{-1}$), and increases with the orientational ordering of particles (when $h(\phi)$ has a certain structure). The opposite occur with the excess part of the free-energy $\Phi_{\rm 2D}$, which decreases with the orientational ordering of particles, because as we have pointed out before, the excluded area has its absolute minimum for parallel particle configurations. Thus for a fixed density ρ the final equilibrium profile $h_{\rm eq}(\phi)$ is given from the total free-energy minimization taking into account both contributions. If ρ is small enough the equilibrium distribution is uniform consistent with random orientations of particle axes, the so called isotropic (I) liquid-crystal phase. If ρ is high enough, for any value of the aspect ratio κ, the equilibrium distribution $h(\phi)$ is peaked around $\phi = 0$ and $\phi = \pi$, the so called uniaxial nematic (N) liquid-crystal phase. The direction along which the particle axes are aligned is called the nematic director. Finally if κ is relative small (as we will see below when $\kappa \in$ [1,2.62]) increasing ρ we find that the I phase exhibits a transition to the so called tetratic or 4-atic phase (a phase with fourfold symmetry, i.e. invariant under $\pi/2$-rotation). Now exists two mutual perpendicular equivalent directions (the so-called tetratic directors) of preferential orientational ordering of particles. This phase in turn can be stable only if the $A^{\rm (spt)}(\phi)$ has a local minimum at the relative angle $\phi = \frac{\pi}{2}$ and the difference between the local and absolute minima are relatively small, as it is shown in Fig. 18 for hard rectangles with $\kappa = 2$. Note that for $\kappa = 1$ (hard squares) all minima at $\{0,\pi/2,\pi\}$ are equivalent which is consistent with the four-fold symmetry of squares. This in turn means that the unique orientationally ordered phase of hard squares is the tetratic phase. We plot in the inset of Fig. 19 the equilibrium distribution functions $h(\phi)$ as obtained from the solutions of Eq. (77) for different values of η selecting $\kappa = 2$. Note the tetratic or uniaxial nematic symmetries of $h(\phi)$ for certain medium and high values of η respectively, while $h(\phi) = (2\pi)^{-1}$ (the I phase) for the small value of η. For the nematic and tetratic phases we have the symmetries $h(\phi + \pi) = h(\phi)$ and $h(\phi + \pi/2) = h(\phi)$ respectively.

To find the boundaries of phase transitions between phases with different symmetries we firstly need to define the uniaxial nematic (Q_2) and tetratic (Q_4) order parameters:

$$Q_n \equiv \int_0^{2\pi} d\phi h(\phi) \cos(2n\phi), \quad n = 1,2, \tag{79}$$

These order parameters $Q_n \in [0,1]$ are a meassure of the degree of orientational ordering of particles in the nematic ($n = 1$) and tetratic ($n = 2$) phases. For the tetratic phase $Q_4 > 0$ while $Q_2 = 0$, for the nematic phase $Q_2 > Q_4 > 0$ and finally for the isotropic phase $Q_2 = Q_4 = 0$.

If I-N or I-T transitions are of second order we obtain that decreasing η from the region of stability of N or T phases we have that $\lim_{\eta\to\eta^*} Q_2(\eta) = 0$ and $\lim_{\eta\to\eta^*} Q_4(\eta) = 0$ respectively, defining in such a way the value of packing fraction η^* at the second-order phase transition. In case of first order phase transition we need to solve the equations that guarantee the chemical and mechanical equilibrium, i.e. the equality of the chemical potentials and pressures between the coexisting phases. The chemical potential, $\beta\mu$, and pressure, βp, following the SPT, are given by

$$\beta\mu = \frac{\partial\Phi_{2D}^{(tot)}}{\partial\rho} = \ln\left(\frac{\rho}{1-\eta}\right) + \int_0^{2\pi} d\phi h(\phi) \ln h(\phi) + \frac{2\rho^{-1}\langle\langle A^{(spt)}\rangle\rangle}{1-\eta} + \beta pa, \tag{80}$$

$$\beta pa = \rho\,(\beta\mu) - \Phi_{2D}^{(tot)} = \frac{\rho}{1-\eta} + \frac{\langle\langle A^{(spt)}\rangle\rangle}{(1-\eta)^2}. \tag{81}$$

Thus we need to solve for

$$\mu(\rho_\alpha) = \mu(\rho_\gamma), \quad p(\rho_\alpha) = p(\rho_\gamma) \tag{82}$$

together with Eq. (77) to find the equilibrium values ρ_α, ρ_γ, $h_\alpha(\phi)$ and $h_\gamma(\phi)$ at two-phase coexistence between phases α and γ which could be I, N, and T phases. The phase boundaries $\eta(\kappa)$ of the phase diagram of a hard rectangle fluid were calculated in Ref. [17] and are shown in Fig. 19. The bifurcation boundaries for the I-N and I-T second order phase transitions can be calculated analytically from the so called bifurcation analysis. The later consist on the following: Firstly we take the first order approximation of the Fourier expansion of the orientational distribution function:

$$h(\phi) = \frac{1}{2\pi}\left[1 + h_n \cos(2n\phi)\right], \quad n = 1,2, \tag{83}$$

where h_n are the Fourier amplitudes of the N ($n = 1$) or T ($n = 2$) incipient developed (from I) phase close to the bifurcation point η_n^*. Inserting this expression into the Eq. (77) and expanding it with respect to h_n up to first order we obtain an equation of the form $A(\eta,\kappa)h_n = 0$ which has a non trivial solution at bifurcation if $A(\eta_n^*,\kappa) = 0$. This allows us to find $\eta^*(\kappa)$. Its explicit expression is

$$\eta_n^*(\kappa) = \left[1 + \frac{2\left(\kappa + \kappa^{-1} + 2(-1)^n\right)}{(4n^2-1)\pi}\right]^{-1}, \quad n = 1,2. \tag{84}$$

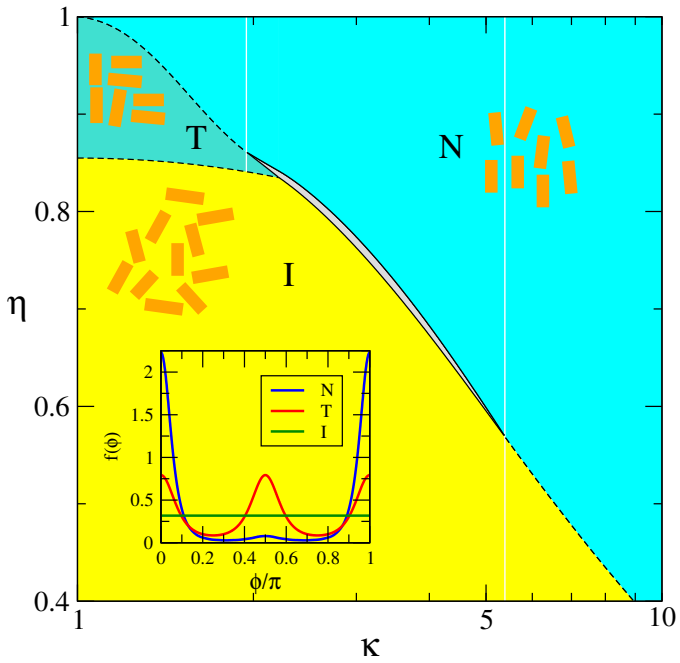


Figure 19: Phase diagram of the HR fluid considering only uniform phases in the packing fraction, η, vs. aspect ratio, κ, plane. Regions of stability of I, N and T phases are correspondingly labeled. With solid and dashed lines we show first and second order phase transitions. The shaded gray region is the I-N instability region. Three sketches of configurations of particles with I, N and T orientational symmetries are also shown. Inset: Equilibrium orientational distribution functions corresponding to I (green), T (red) and N (black) symmetries are shown for some selected low, medium and large values of η.

The equality $\eta_1^*(\kappa) = \eta_2^*(\kappa)$ gives the value at which the I-N and I-T bifurcation curves intersect which result in $\kappa^* = \dfrac{3+\sqrt{5}}{2} \approx 2.62$. For $\kappa < \kappa^*$ the I phase exhibits a second order phase transition to the T phase while for $\kappa > \kappa^*$ the I bifurcates to the N phase. However as we can see from Fig. 19 the I-N phase transition is of first order up to the aspect ratio corresponding to the first tricritical point $\kappa_t^{(1)} \approx 5.44$ beyond which (for $\kappa > \kappa_t^{(1)}$) a second order I-N transition takes place, while for $\kappa < \kappa_t^{(1)}$ it is of first order. It can be seen in Fig. 19 that there exists an small interval of aspect ratios $[\kappa_t^{(2)},\kappa^*]$ where a first order T-N transition occurs while for lower values than that corresponding to a second tricritical point $\kappa_t^{(2)} \approx 1.94$ the T-N transition is of second order. The later T-N bifurcation boundary can be calculated only numerically trough a bifurcation analysis similar to that described above.

The SPT can be extended to general mixtures of hard particles with the same expression (72) for Φ_{2D} with the following generalization of the double angular average of the spt-area:

$$\langle\langle A^{(\mathrm{spt})}\rangle\rangle = \sum_{i,j=1}^{c} \int_0^{2\pi} d\phi_1 \int_0^{2\pi} d\phi_2 \rho_i(\phi_1)\rho_j(\phi_2) A_{ij}^{(\mathrm{spt})}(\phi_{12}), \tag{85}$$

where the mixture is constituted by c different species with number density distribution functions $\{\rho_i(\phi)\}$, while the excluded areas between species i and j, $A_{ij}^{(\mathrm{exc})}(\phi_{12})$, are the inputs of the theory.

With this generalization we can study the stability of a general binary mixture of hard bodies

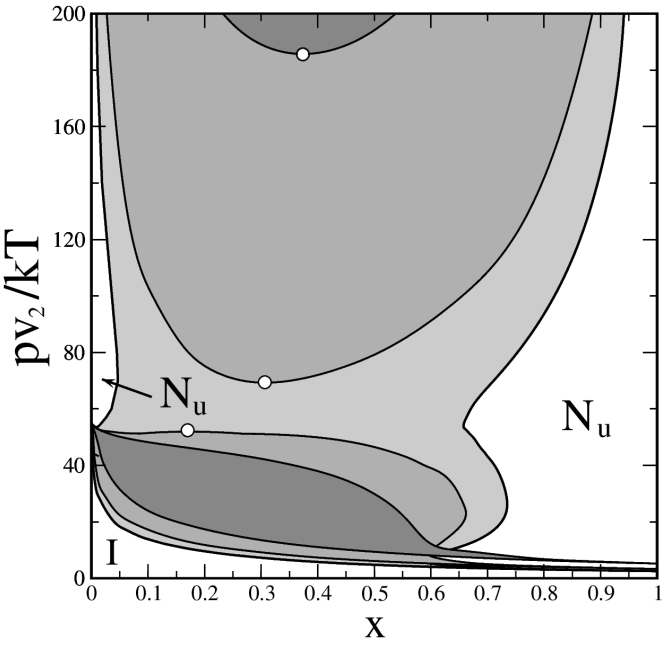


Figure 20: Phase diagram in the pressure, βp, vs. composition x (of the large component 1) plane. The width of both species are the same while their aspect ratios are $\kappa_2 = 1$ and $\kappa_1 = 4,\ 4.6$ and 5. The zones of stability of different phases are correspondingly labeled. Empty circles we show the positions of critical points.

in 2D with respect to phase separation between two different phases. It was shown that the SPT does not allow demixing between two I phases [18, 19]. However we have found I-N or N-N demixing in binary mixtures of HR as it is illustrated in Fig. 20, where we plot the phase diagram in the pressure (see Eq. (81) βp vs. the molar fraction of the large component plane. We define this molar fraction as $x = x_1 \equiv \rho_1/\rho$ ($\rho_i = \int_0^{2\pi} d\phi \rho_i(\phi)$, $\rho = \sum_i \rho$). Both species have the same width σ but different aspect ratios: $\kappa = 2$ and $\kappa_1 = 4,\ 4.6$ and 5. For $\kappa_1 = 4$ and 4.6 apart from the I-N transition we found a N-N demixing at high pressures ending at critical points (white circles), where the zones of instability with respect to phase separations are shades in gray. For $\kappa_1 = 4.6$ we have a upper critical point of the I-N demixing region. However for $\kappa_1 = 5$ the critical points disappear and we get a unique demixing region separating phases (I or N) each one rich in one of the components.

2.6 Fluid of hard isosceles triangles (HT)

As another example of the SPT implementation to study the liquid crystal phase behavior of two-dimensional hard particle fluid we select the isosceles triangular geometry. The particles now has a triangular shape with three edge-lengths two of which are equal and they converge to the vertex of opening angle α. The main triangular axis is parallel to the height pointing from the triangular base to the vertex with opening angle α. The unique magnitude we need to implement calculations from the SPT-formalism is the excluded area (see Fig. 21 (a) for its sketch). We do not provide here its analytic expression which can be found in Ref. [?]. In Fig. 21 (b) we plot three examples of the spt-area, $A^{(\mathrm{spt})}(\phi)$, for the equilateral triangle ($\alpha = \pi/3$), the right triangle

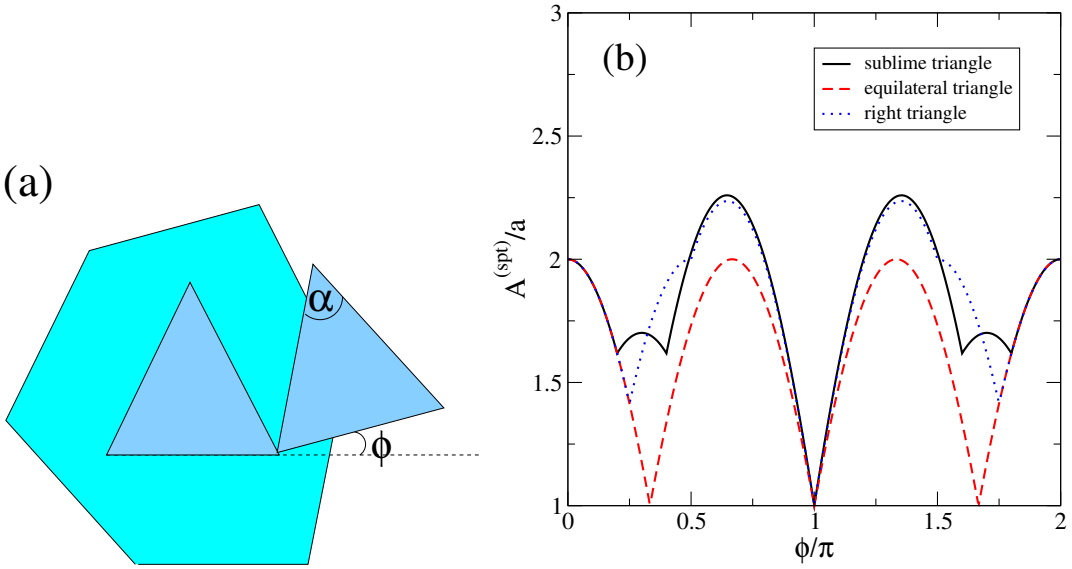


Figure 21: (a): Sketch of the excluded area between two isosceles triangles (of certain opening angle α) for a given relative orientations of particle axes: the vectors parallel to the heights pointing from the bases of triangles to the vertex of opening angle α. (b): The spt-area for the equilateral, right-angled, and sublime triangles, the later defined as the isosceles triangle with the ratio between its equally sized length and the base being equal to the golden ratio $\varphi = \dfrac{1+\sqrt{5}}{2}$.

($\alpha = \pi/2$) and the sublime triangle, defined as the isosceles triangle with the ratio between the equally sized length and base being equal to the golden number $\varphi = \frac{1+\sqrt{5}}{2}$. As we can see the spt-area has in general a complex form with many local minima and maxima. In particular that for the equilateral triangle has three equivalent absolute minima in the interval [0,2π] separated by $2\pi/3$, which in turn means that one of the stable liquid crystal phase should has a six-fold symmetry, the so called 6-atic phase with orientational distribution function invariant under $\pi/3$ rotation, i.e. $h(\phi = h(\phi + \pi/3)$. One example of $h(\phi)$ is shown in Fig. 22 (a) (dashed line) for triangles with an opening angle α close, but no equal to, $\pi/3$ and for a value of η inside the stability window of the 6-atic phase. See how $h(\phi)$ has three equivalent peaks at 0 (or π, the same peak), $\pi/3$ and $2\pi/3$. For a value of η bit higher, just when the 6-atic phase is unstable, we found the usual N phase with orientational distribution function with the usual symmetry $h(\phi) = h(\phi + \pi)$ as it is shown in Fig. 22 (a). For low enough values of η the I phase, with uniform orientational distribution function, is the stable phase. Note that the order parameter Q_3 defined by Eq. (79) specified for $n = 3$ is the one required to measure the 6-atic orientational ordering of particles.

The phase diagram, as it was presented in Ref. [20], is plotted in Fig. 22 (b) in the packing fraction, η, opening angle, α, plane. The regions of stability of I, N, and 6-atic phases are labeled. The blue and red curves represent the second and first order transition boundaries. The I–6-atic and I-N second order curves $\eta(\alpha)$ can be obtained analytically from the bifurcation analysis as explained above. We write down the explicit expression for this function:

$$\eta_n^*(\alpha) = \left[1 + \frac{4}{(4n^2-1)\pi} \cdot \frac{(\sin(\alpha/2) - \cos(n\alpha))^2}{\sin\alpha}\right]^{-1}, \quad n = 1,3. \tag{86}$$

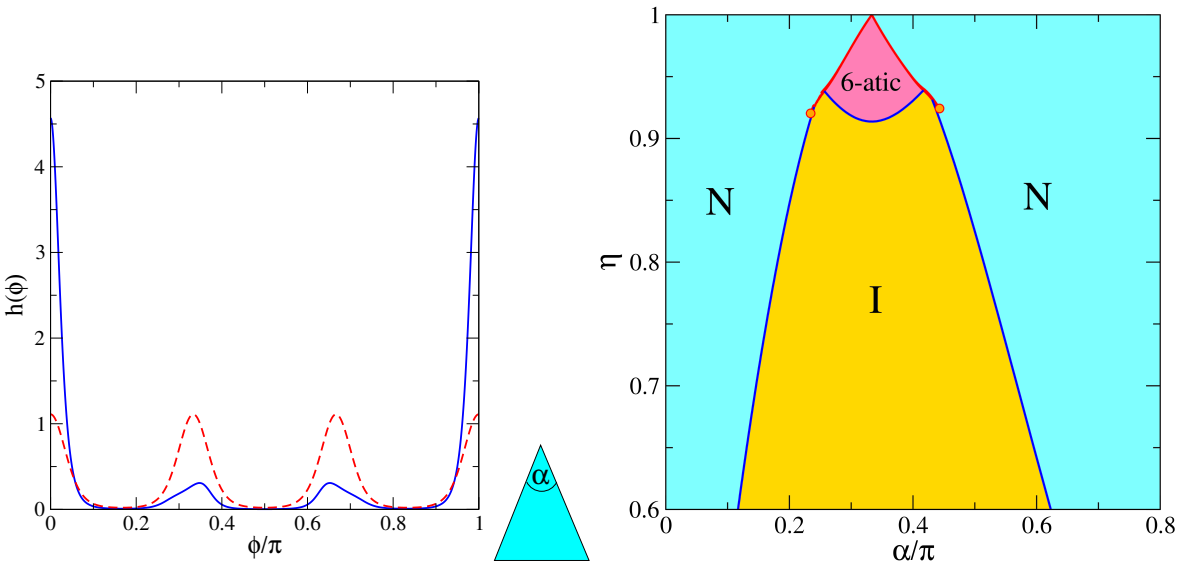


Figure 22: Left: Orientational distribution functions $h(\phi)$ corresponding to N (solid line for $\eta = 0.95$) and 6-atic (dashed line for $\eta = 0.949$) phases of triangles with opening angle $\alpha = 48.9°$. Right: Phase diagram in the packing fraction η vs. the opening angle of the isosceles triangles α. The regions of stability of I, N and 6-atic phases are correspondingly shown. Blue and red curves correspond to second and first order phase transitions respectively.

The equality $\eta_1^*(\alpha) = \eta_3^*(\alpha)$ gives us an equation to find the angles α_i^* $(i = 1,2)$ which define the interval of opening angles $[\alpha_1^*,\alpha_2^*]$, enclosing the 60°-equilateral angle, inside which the 6-atic phase is stable (except in the case of first order (I,T)-N transitions) for certain values of η beyond the bifurcation value η_3^*. We found $\alpha_1^* = 45.16°$ and $\alpha_2^* = 76.07°$, so the 6-atic phase could be stable in a window of opening angles around 60° of width $\Delta\alpha^* \equiv \alpha_2^* - \alpha_1^* = 30.91°$. The coexistence calculations to find the first-order boundaries were calculated as explained in the preceding section.

2.7 Monte Carlo method for anisotropic hard particles

The equilibrium Monte Carlo (MC) method is ideally suited to studying hard-body models in general, and anisotropic models in particular. MC codes are easy to implement, but the results have to be analysed carefully. In this section we give a brief introduction to the topic, discussing the basic approaches and algorithms, and finally present a nontrivial particle model in 2D.

In the MC method the basic configurational variables of the N particles are taken as random variables. For example, for a 2D particle system, we have to specify N sets of variables, each consisting of the position of the particle, $\boldsymbol{r} = (x,y)$, and the orientation of the long particle axis, given by an angle ϕ with respect to a fixed axis, say the x axis. Then we have the $3N$ random variables

$$\boldsymbol{\xi}_i = (\boldsymbol{r}_i,\phi_i), \quad i = 1,2,\cdots,N, \tag{87}$$

and specific values for these variables characterize a particular configuration of the system in configuration space,

$$\boldsymbol{\xi} \equiv (\boldsymbol{\xi}_1,\boldsymbol{\xi}_2,\cdots,\boldsymbol{\xi}_N). \tag{88}$$

An observable G is calculated by averaging the desired quantity g (defined for each configuration) over many representative configurations of the system:

$$G = \langle g \rangle \simeq \frac{1}{M}\sum_k g(\boldsymbol{\xi}_k), \tag{89}$$

where M is the number of configurations. By 'representative' we mean configurations with a sufficiently large value of the configurational probability function $P(\boldsymbol{\xi})$, with

$$P(\boldsymbol{\xi}) \propto e^{-\beta\mathcal{H}(\boldsymbol{\xi})}, \tag{90}$$

where $\mathcal{H}(\boldsymbol{\xi})$ is the Hamiltonian. We use the symbol 'proportional to', as the normalization of the probability $P(\boldsymbol{\xi})$ is just the partition function Z_N, which is unknown (otherwise all the thermodynamic properties of the system could be calculated by differentiating the free energy $F = -kT\log Z_N$, and we would not even consider doing simulations).

The problem is: how can we generate representative configurations, when we cannot even know the probability function? There are many methods to sample probability distribution functions, but: (i) here we have many degrees of freedom, (ii) in principle, knowledge of the full probability function is required. It turns out that there are methods to sample a probability distribution function that do not require the normalization of the function to be known. One of these methods is the so-called *Metropolis algorithm*.

In this method, we define a Markov chain: a sequence of configurations,

$$\boldsymbol{\xi}^{[0]}, \boldsymbol{\xi}^{[1]}, \cdots, \boldsymbol{\xi}^{[k]}, \cdots \tag{91}$$

where the elements are uncorrelated. We need to specify an algorithm to obtain $\boldsymbol{\xi}^{[k+1]}$ from $\boldsymbol{\xi}^{[k]}$, with the constraint that the set of generated configurations be distributed according to the probability distribution function $P(\boldsymbol{\xi})$. This is accomplished as follows. We choose one particle, with label l, sequentially or at random, and perform a trial move, which will be accepted or not. We repeat the process N times, visiting all N particles or choosing particles N times. In each stage, the coordinates of the lth particle are changed as

$$\boldsymbol{r}_l' = \boldsymbol{r}_l + \chi\Delta\boldsymbol{r}, \quad \phi_l' = \phi_l + \eta\Delta\phi, \quad \boldsymbol{\xi}_l' = (\boldsymbol{r}_l',\phi_l'), \tag{92}$$

where $\Delta\boldsymbol{r}$ and $\Delta\phi$ are small quantities, with values set at the beginning (although they can be adjusted during the simulation), and $\chi,\eta \in [-1,1]$ are uniformly distributed random variables. The advanced configuration (which only involves changes in one particle) is accepted with a

probability r, with

$$r = \frac{P(\boldsymbol{\xi}_1^{[k]}, \cdots, \boldsymbol{\xi}_{l-1}^{\prime[k]}, \boldsymbol{\xi}_l^{\prime[k]}, \boldsymbol{\xi}_{l+1}^{\prime[k]}, \cdots, \boldsymbol{\xi}_N^{[k]})}{P(\boldsymbol{\xi}_1^{[k]}, \cdots, \boldsymbol{\xi}_N^{[k]})}. \tag{93}$$

Accepting the move with probability r means: we sort a uniformly random number $\gamma \in [0,1]$. If $r < \gamma$ the move is accepted; otherwise it is rejected. Then we update the configuration of the lth particle as

$$\boldsymbol{\xi}_l^{[k+1]} = \begin{cases} \boldsymbol{\xi}_l^{\prime[k]} & \text{if the move is accepted} \\ \boldsymbol{\xi}_l^{[k]} & \text{if the move is not accepted} \end{cases} \tag{94}$$

We then repeat the process N times, each time making a trial move which is accepted using the same algorithm. After this, we say that we have completed a Monte Carlo step, which means moving the whole system to a new configuration $\boldsymbol{\xi}^{[k]} \rightarrow \boldsymbol{\xi}^{[k+1]}$. We perform M Monte Carlo steps.

It can be shown that the sequence of configurations so generated tends to the Boltzmann distribution $P(\boldsymbol{\xi})$ in the asymptotic limit $M \rightarrow \infty$. This means that a 'warming' sequence is required to enter a regime where the generated configurations get distributed according to $P(\boldsymbol{\xi})$ as closely as possible. After this sequence, we can consider to have entered the 'equilibrium' stage from the 'equilibration' stage, and use the configurations generated henceforth to calculate statistical averages.

A few comments are in order:

- How can we know that we have reached the 'equilibrium' stage? We can monitor the behaviour of one or more quantities along the simulation. When they set to constants values, or at least begin to fluctuate about a constant value, we can be sure that the equilibrium stage has been reached.

- Reaching the equilibrium stage is not enough: we have to average over many 'equilibrium' configurations once the equilibrium stage is entered.

- How can we optimize things so as to reach the 'equilibrium' stage as sooner as possible? This is not easy, but it helps if we prepare the initial configuration to be as representative as possible of the equilibrium situation. It may be difficult to guess such a configuration, because we may not know the stable configurations of the system in the first place.

- What happens with the partition function? Since the basic quantity is the probability r, which is given by the *ratio* between the probabilities, the partition function is not needed, as it does not enter into the process. This is very convenient and in fact one of the strong points about the algorithm.

- Is is convenient to run a few simulations from different initial conditions $\boldsymbol{\xi}^{[0]}$? Not in principle, as the history of the system is lost as we make progress into the simulation towards the equilibrium stage. But sometimes the systems are frozen in some special

configuration, and we may have to try different initial configurations in order to overcome this problem.

2.8 N-particle system of hard-rod particles

In this example we apply the Monte Carlo method to sample an N-particle system of confined hard-rod particles in 1D. This is a particularly simple case with a simple overlap condition. The reason why we consider a confined system is that hard rods cannot order into crystalline phases (and oriented ones are of course discarded because of the reduced dimensionality). Because of particle interactions and correlations, a confined fluid of hard rods does not arrange into a uniform phase with constant local density across the total length, but form a stratified structure, with oscillations next to the walls that propagate into the centre of the confining cavity.

We consider Fig. 23, where a schematic of the system is shown. The distance between the walls is H. Rods are of length σ. The l parameter gives the free length between consecutive rods (note that rods labels are ordered, as rods can not overcome one another) in the initial configuration, where rods are equally spaced. The packing fraction of the system is given by

$$\eta = \frac{N\sigma}{H}. \tag{95}$$

In the initial configuration

$$H = N(\sigma + l) \quad \rightarrow \quad l = \frac{1-\eta}{\eta}, \tag{96}$$

with N the number of rods. Initially we distribute the rods uniformly along the simulation box,

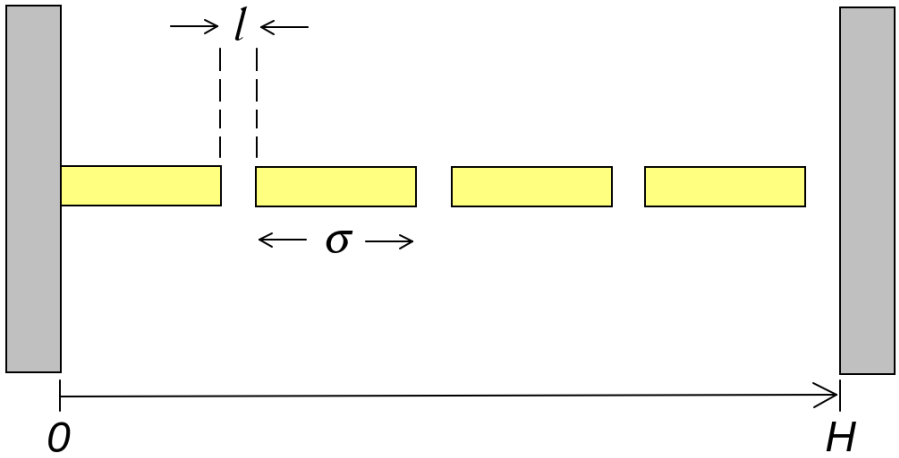


Figure 23: Geometry for the Monte Carlo simulation of confined hard rods. H is the separation between plates. l is the free length between the rods at the initial configuration (or the mean rod free distance).

at positions $x_i = \sigma/2 + (i-1)(\sigma + l)$, $i = 1,2,\cdots,N$. The box length will then be $H = N(\sigma + l)$. The algorithm is the following. In each Monte Carlo step, we visit all N rods sequentially, trying

to move the rods randomly within some interval Δx. Therefore, the test position of a rod is

$$x_i' = x_i + \Delta x \xi, \quad \xi \in [-1,1], \tag{97}$$

where ξ is chosen from a uniform distribution (in the computer we can evaluate ξ with the expression `2*rand()-1`). We then check whether the new position leads to an overlap with either wall or with the two neighbours. The latter are always the same, so the overlap condition is easy and fast to evaluate. The move is accepted if no overlap results. Otherwise it is rejected and the new configuration is taken to be the same as the previous one. We sweep over all N particles, each time repeating the process. Once completed, we have made one Monte Carlo step. The value of Δx is adjusted so as to give an acceptance ratio of approximately 50%.

Fig. 24 shows the histogram of the density profile for the case $\eta = 0.77$, which results in a wall separation of $H = 19.48\sigma$. Note the strong stratification of the rods next to the wall: rods tend to pile up at the wall, which generates a region of low probability next to rods (at the right of the rod on the left, and at the left of the rod on the right). This effect propagates into the centre of the cavity due to multi-particle correlations. The effect is particularly pronounced at high densities and small separations between the walls. In higher dimensionalities this effect is a precursor of ordering transitions (which do not exist in the hard-rod system).

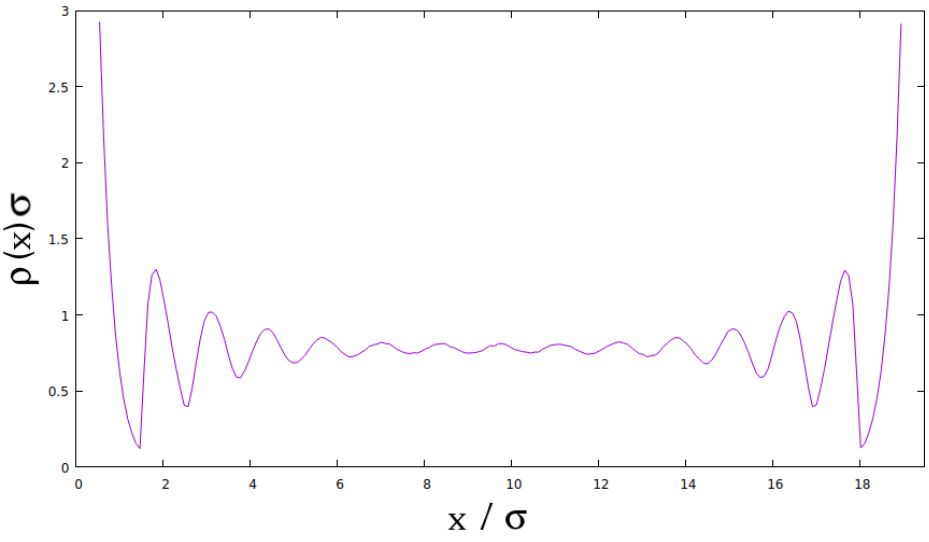


Figure 24: Equilibrium density profile for a confined hard-rod fluid. $H = 19.48\sigma$. The packing fraction is $\eta = 0.77$.

3 Vibrated granular monolayers and elastic theory

In this section we make a transition from thermal equilibrium systems to granular systems. We will see that hard-particle models may be very good models to analyse granular materials. Also, under some conditions, granular monolayers can be excited so that their behaviour is very similar to that of standard equilibrium condensed matter.

3.1 Introduction

Granular material consist of grains, i.e. particles that are approximately hard and that are subject to energy scales (typically given by external forces) many order of magnitude larger than thermal energies k_BT. Therefore, they are athermal, and their properties are not controlled by thermal fluctuations, but by external forces and constraints. In this sense, granular 'fluids' are not molecular fluids, but a different entity. Topics such as dissipation and friction, external driving, force chains and granular temperature, and maximum packings, all of them alien to the equilibrium world, are central in the discussion of granular systems.

However, in this course we will not cover these important aspects of granular matter. We will rather concentrate on some specific behaviours of granular monolayers than can be exploited to extract information on similar 2D equilibrium systems subject to thermal fluctuations. It turns out that a vertically-vibrated quasimonolayer of particles behaves in ways similar to their equilibrium counterparts. In particular, they can form oriented fluid fluids and, when subject to confinement and to geometrical frustation, they form topological defects to restore the symmetry of the fluid phase. These defects can be characterised by means of topological charges that follow conservation rules. In order to proceed, we will first delve into the theory of elasticity in 2D nematic fluids.

3.2 Elastic Theory for 2D nematics

Consider a two-dimensional liquid crystal fluid made of particles that locally orient in average along the so-called nematic director which could be a nonuniform function of the spatial variables $\boldsymbol{r} = (x,y)$. The nematic director is defined as the two-dimensional unit vector

$$\boldsymbol{n}(\boldsymbol{r}) = [\cos\theta(\boldsymbol{r}), \sin\theta(\boldsymbol{r})]\,, \tag{98}$$

with $\theta(\boldsymbol{r})$ the angle that the director form with respect to the x-axis of a fixed reference frame. The fact that the nematic director deforms, departing from its uniform character in equilibrium at bulk conditions, implies the existence of an energy cost. This one is classified in the following two-types, depending, on the symmetries of its deformations: (i) the splay distortion mode, proportional to the square of its divergence, $\sim (\mathrm{div}\,(\boldsymbol{n}))^2$, and the bending distortion mode, proportional to the square of the cross product between the director and its rotational, $\sim (\boldsymbol{n} \times \mathrm{rot}\,(\boldsymbol{n}))^2$. Thus, the elastic free-energy is defined as the integral, over the whole system, of the sum of both contributions multiplied by the so called splay, K_1, and bend, K_3, elastic

constants [21]:

$$F_{\rm el}[\boldsymbol{n}] = \frac{1}{2}\int_A d\boldsymbol{r}\left\{K_1\left[\mathrm{div}(\boldsymbol{n}(\boldsymbol{r}))\right]^2 + K_3\left[\boldsymbol{n}(\boldsymbol{r})\times \mathrm{rot}(\boldsymbol{n}(\boldsymbol{r}))\right]^2\right\}, \tag{99}$$

with A the total area of the system.

Using the one-constant approximation $K \equiv K_1 = K_3$, and inserting the expression (98) into (99) we obtain

$$F_{\rm el}[\theta] = \frac{K}{2}\int_A d\boldsymbol{r}\,|\boldsymbol{\nabla}\theta(\boldsymbol{r})|^2\,. \tag{100}$$

The functional minimization of (100) with respect to $\theta(\boldsymbol{r})$ provides the Euler-Lagrange equation for the field $\theta(\boldsymbol{r})$: $\Delta\theta(\boldsymbol{r}) = 0$. Suppose now that the nonuniform character of the field $\theta(\boldsymbol{r})$ is produced by the presence of a single *defect* positioned at $\boldsymbol{r} = 0$ where the vector field $\boldsymbol{n}$ has a singularity. It is clear, from the symmetry conditions, that if we encircle the defect along a closed path γ, the total change in the angle $\theta(\boldsymbol{r})$ should coincides with the angle corresponding to the p-atic symmetry of the liquid crystal fluid, i.e. $\pm 2\pi/p$. Remember that a p-atic fluid is that which is invariant with respect to a $2\pi/p$-rotation. Thus we have

$$\oint_\gamma d\theta = \pm\frac{2\pi}{p} = 2\pi w. \tag{101}$$

The sign $\pm$ corresponds to the sign of the *topological charge* of the defect. Usually the number $w = \pm 1/p$ is called the winding number of the defect.

It is clear that, in polar coordinates $(x,y) = (r\cos\phi, r\sin\phi)$, the solution where the angle θ is a linear function of ϕ (satisfying (101)) in fact satifies the equation $\Delta\theta = 0$. Thus we have $\theta = \theta_0 + w\phi$, with θ_0 an integration constant. Consequently we have

$$\boldsymbol{\nabla}\theta = \frac{\partial\theta}{\partial r}\boldsymbol{e}_r + \frac{1}{r}\frac{\partial\theta}{\partial\phi}\boldsymbol{e}_\phi = \frac{w}{r}\boldsymbol{e}_\phi, \tag{102}$$

with $\boldsymbol{e}_r$ and $\boldsymbol{e}_\phi$ the unit vectors along the radial and angular directions. Substituting (102) into (100) we arrive at

$$F_{\rm el} = \frac{Kw^2}{2}\int_0^{2\pi} d\phi\int_a^R dr\frac{1}{r} = \pi K w^2 \log\left(\frac{R}{a}\right), \tag{103}$$

where a is a lower cut-off that avoid the singularity ar $r = 0$ which represents the effective dimension of the core of the deffect, while R is the linear dimension of the system. This expresion, being always positive, shows that indeed an energy cost exist when a defect of the field $\boldsymbol{n}$ is created and also that the free-energy has a logarithmic grow with the system size.

An important use of the elastic theory is that we can calculate the curves which tangent lines coincides with the orientations of the director corresponding to a liquid-crystal phase with p-fold

symmetry (the p-atic phase). To this purpose note that we only need to solve the equation

$$\frac{dy}{dx} = \frac{r'(\phi)\sin\phi + r(\phi)\cos(\phi)}{r'(\phi)\cos(\phi) - r(\phi)\sin(\phi)} = \tan(\theta(\phi)) = \tan(w\phi + \theta_0). \tag{104}$$

The solution of this equation is

$$r(\phi) = r_0 \left|\sin\left[(w-1)\phi + \theta_0\right]\right|^{1/(w-1)}. \tag{105}$$

where r_0 is a new integration constant. Selecting different values of $\theta_0^{(i)}$ $(i = 1,2,\ldots,p/2)$ which differences are compatible with the p-atic symmetry of the liquid crystal phase, i.e. $\theta_0^{(i)} - \theta_0^{(j)} = 2\pi/p$ and also different values of r_0 (the distance from the defect position) we can generate several tangent curves in the $x-y$ plane [with $(x,y) = (r(\phi)\cos\phi, r(\phi)\sin(\phi))$].

For example selecting $\theta_0 = 0$, $p = 2$ (the usual uniaxial nematic phase) and $w = \pm\frac{1}{2}$, we obtain , as shown in Fig. 25, the director field orientation corresponding to the usual dipole-like defects. To illustrate how change the director when we surround the defect along any closed curve γ, we particularized γ to be a circumference (shown in red) and draw with blue bars the tangents to the $\pm\frac{1}{2}$-curves at the intersections between them and the circumference. We can see that the director orientation θ has a total variation of $2\pi w = \pi$ for $w = +1/2$ when we surround the defect counter clockwise (yellow arrow) while it is equal to $2\pi w = -\pi$ for $w = -1/2$. The same

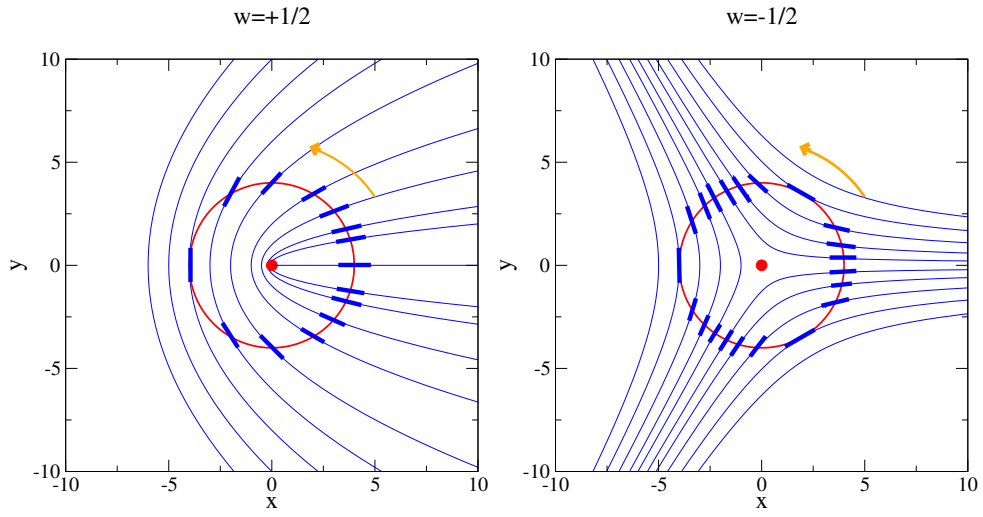


Figure 25: The director field around a point-like defect of winding numbers $w = +1/2$ (left)and $-1/2$ (right). Different orientations (blue bars) of the director at the intersections between the $\pm 1/2$-curves and a circumference (shown in red) are indicated.

representation can be carried out for $p = 4$ (the tetratic symmetry produced by a fluid of hard rectangles), selecting $w = \pm 1/4$, and $\theta_0^{(1)} = 0$, $\theta_0^{(2)} = \pi/2$ with the result shown in Fig. 26. Now exists two equivalent mutual perpendicular directors (shown with blue and green bars at the intersections between the $\pm 1/4$-curves and the circumference). Note how θ change $2\pi w = +\pi/2$ (for $w = +1/4$) or $2\pi w = -\pi/2$ (for $w = -1/4$) as we surround the defect counter clockwise. Finally, selecting $\theta_0^{(1)} = 0$, $\theta_0^{(2,3)} = \pm\pi/3$ (corresponding to $p = 6$), and $w = \pm 1/6$, we obtain the director field corresponding to a 6-atic liquid crystal phase (that stabilized by a fluid of the

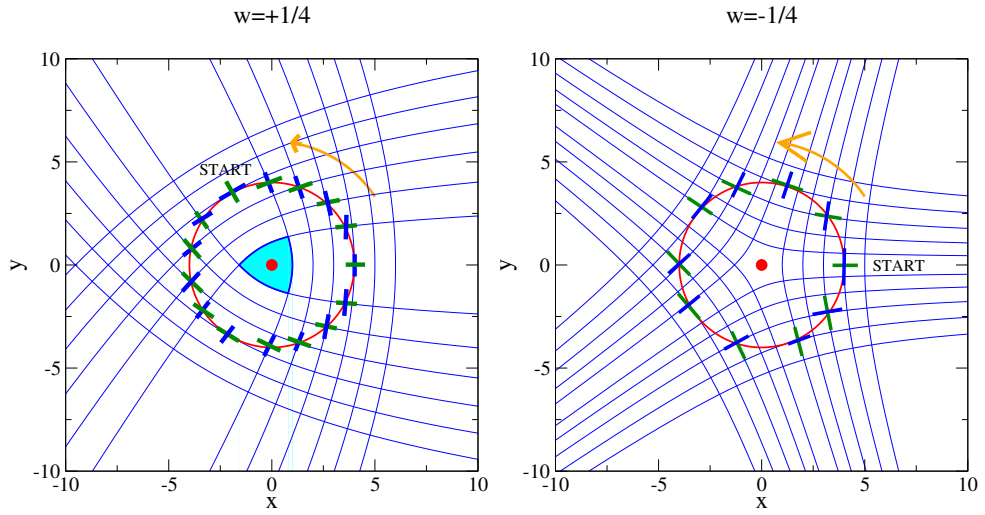


Figure 26: The director field around a point-like defect of winding numbers $w = +1/4$ (left)and $-1/4$ (right). Different orientations (blue and green bars) of the director at the intersections between the $\pm 1/4$-curves and a circumference (shown in red) are indicated.

equilateral triangles). The results are shown in Fig. 27. Now exists three equivalent directors, each one rotated $\pm 2\pi/3$ with respect to its neighbor. The total change in θ, when we surround the defect, is equal to $2\pi w = \pi/3$ (for $w = +1/6$) and $2\pi w = -\pi/3$ (for $w = -1/6$). In case

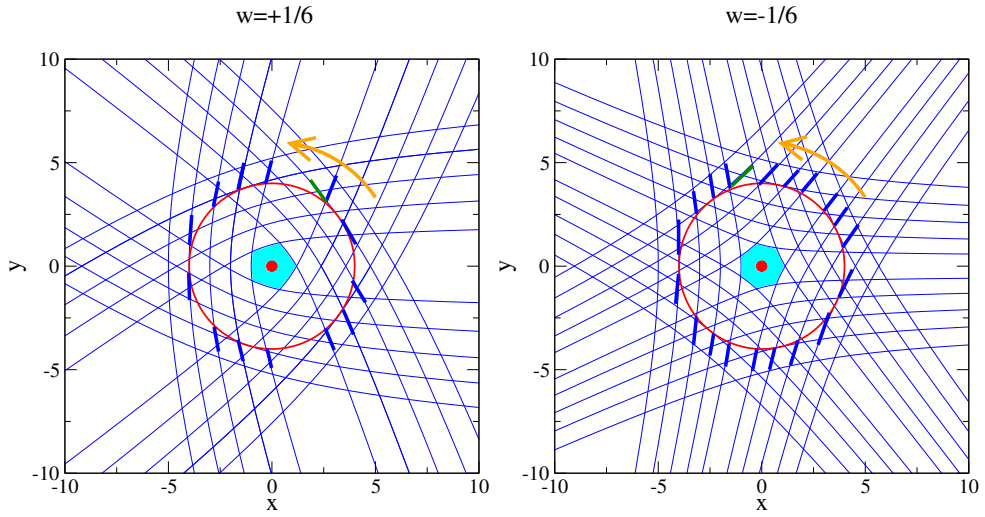


Figure 27: The director field around a point-like defect of winding numbers $w = +1/6$ (left)and $-1/6$ (right). Only one of three equivalent orientations (blue bars) of the director at the intersections between the $\pm 1/6$-curves and a circumference (shown in red) are indicated.

two topological defects of the orientation field are fixed at the positions (x_i,y_i) $(i = 1,2)$ they certainly interact with each other, similar to the interaction between electrostatic charges in two dimensions. Resorting to the superposition principle the total angular variation at any position $\boldsymbol{r} = (x,y)$ is now $\theta(\boldsymbol{r}) = \theta_1(\boldsymbol{r}) + \theta_2(\boldsymbol{r})$, where

$$\theta_i(\boldsymbol{r}) = \arctan\left(\frac{y - y_i}{x - x_i}\right). \tag{106}$$

The elastic energy interaction energy is thus

$$\begin{aligned} F_{\text{el}} &= \frac{K}{2}\int d\boldsymbol{r}\left(\boldsymbol{\nabla}\theta_1(\boldsymbol{r})+\boldsymbol{\nabla}\theta_2(\boldsymbol{r})\right)^2 \\ &= F_{\text{el}}^{(1)}+F_{\text{el}}^{(2)}+K\int d\boldsymbol{r}\boldsymbol{\nabla}\theta_1(\boldsymbol{r})\cdot\boldsymbol{\nabla}\theta_2(\boldsymbol{r}) \\ &= \pi K\left(w_1+w_2\right)^2\log\left(\frac{R}{a}\right)+2\pi K w_1 w_2\log\left(\frac{a}{r_{12}}\right), \end{aligned} \tag{107}$$

where $F_{\text{el}}^{(i)}$ is the elastic energy corresponding to the topological charge i if this were the only one present in the orientational field, while r_{12} is the radial distance between the topological charges 1 and 2. From Eq. (107) we can see that the first term is identically zero for $w_2 = -w_1$, thus the logarithmic divergence with the system size ($R \to \infty$) disappears when the orientational field contains two identical charges of different signs. The second term indicates that topological charges of same sign ($w_1 w_2 > 0$) repeals each other as F_{el} is a decreasing function of r_{12}.

Let us define the topological charge of the defect i as

$$q_i = w_i p, \tag{108}$$

where w_i is its winding number and p indicates the inherent symmetry of the p-atic phase (invariant under $2\pi/p$ rotations). The number of topological charges together with their magnitudes follow a conservative law dictated by topological properties of the surface where the director vector field is embedded. The main topological property of a given surface is defined by its Euler characteristic $\chi \equiv V - E + F$, with V, E and F the number of vertexes, edges and faces of a polygon which tessellates the surface. For example a two-dimensional disk has $\chi = 1$. This conservation dictates that the total sum of topological charges is equal to the product between p and χ:

$$\sum_{i=1}^{N} q_i = p\chi. \tag{109}$$

For example suppose a tetratic ($p = 4$) vector field is embedded inside a disk ($\chi = 1$). We already know that a single isolated defect should has a winding number of $w = +1/4$ and consequently its charge is $q = wp = +1$. Thus we can conclude from Eq. (109) that, considering all defects to be equivalents, i.e. $q_i = q$ for any i, its total number should be equal to $N = 4$. As charges of equal signs repeal to each other the equilibrium configuration of these four equally charged defects should consist in a distribution of defect positions at the vertexes of an inscribed (to the disk) square. This distribution of charges certainly maximizes the distance between them. Suppose now we are in the presence of a 6-atic field ($p = 6$) embedded inside a disk. Thus we have $w = +1/6$ and again $q = +1$. Then Eq. (109) dictates that $N = 6$. The defects should be positioned at the vertexes of a hexagon inscribed in the disk.

This simple elastic theory is expected to work at the continuum limit and under the important assumption that the liquid-crystal fluid is at equilibrium. However as we will promptly see the theory produces correct predictions when we resort to it to explain the behavior of the

liquid-crystal orientational field obtained as stationary states in vibrated monolayers of granular anisotropic particles.

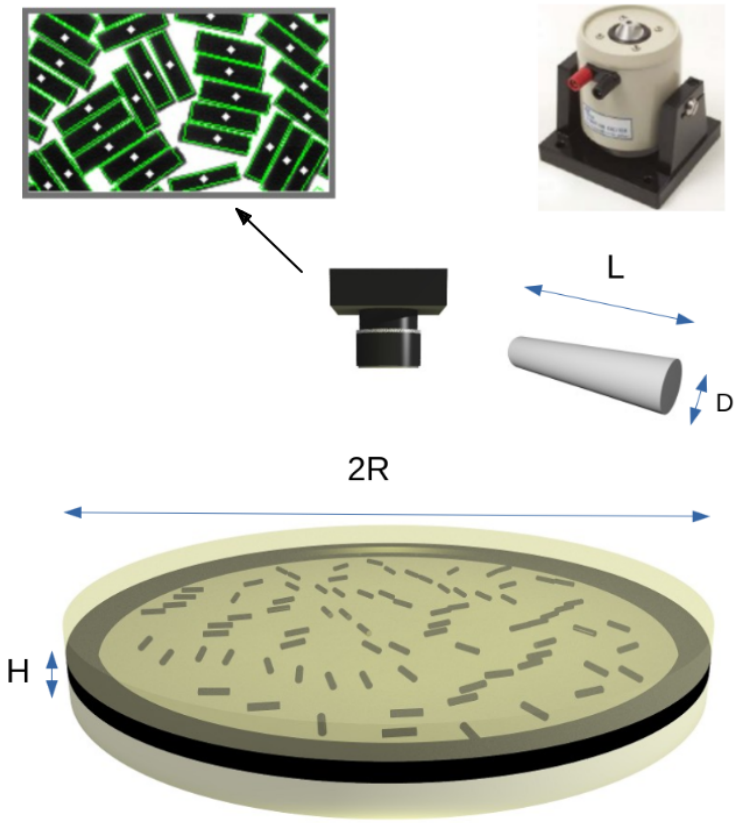


Figure 28: Schematics of the conducted experiments on a vertically vibrated granular monolayer of metallic cylinders. The particle geometry (cylinders of length L and diameter D) is indicated together with an image of the projected cylinders (rectangles) on the horizontal plane. The output from a digital camera is processed to get the positions and orientations of these rectangles. The dimensions of the confining circular cavity are also indicated (its diameter $2R$ and the distance H between the acrylic sheets confining the particles along the vertical direction). A photograph of the electromagnetic shaker used in the experiments is also shown at the top.

3.3 Experiments on vertically vibrated monolayers of granular anisotropic particles

In Fig. 28 we show the experimental setup used to perform the experiments conducted on granular monolayers of cylinders [22]. A granular monolayer of approximately 3000 metallic cylinders of aspect ratio $\kappa = L/D = 4$ are confined into a circular cavity of radius R (with $2R/L = 35$) and between a lower dark plate and upper horizontal acrylic plate with such vertical space between them, H, that only one particle fits ($H/D = 1.8$), but with enough space to allow collisions between the particles and the sheets. The monolayer is vertically vibrated using an electromagnetic shaker operating at certain amplitude a_0 and frequency ν, with effective acceleration $\Gamma = \dfrac{4\pi^2 a_0 \nu}{g} \approx 2$ (with g the gravity constant). The vertical collisions and those between particles produce a two-dimensional effective diffusion of particles inside the cavity. The

images of this non-equilibrium monolayer is taken with a digital camera positioned at zenithal position. These images are processed using a MATLAB code to obtain the lists of positions and orientations of particles and from them to produce the orientational field of rods: the order parameters $Q_2(\boldsymbol{r})$ and $Q_4(\boldsymbol{r})$ measured w.r.t. the 2-atic or 4-atic directors.

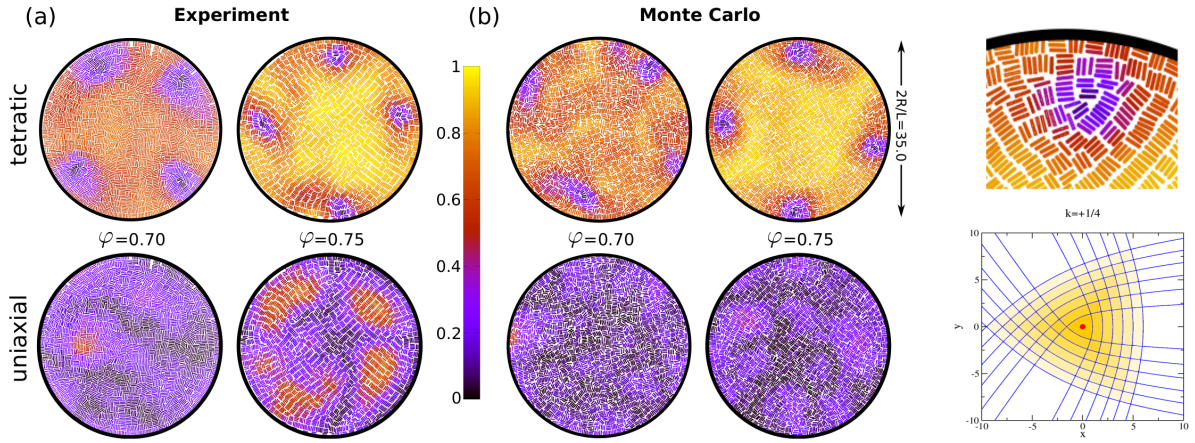


Figure 29: (a): Order parameter fields $Q_2(\boldsymbol{r})$ and $Q_4(\boldsymbol{r})$ shown in color scale as were obtained from experiments on vertically vibrated monolayers of cylinders for two different values of packing fraction φ. Right: Results from MC simulations of a hard rectangle fluid equilibrated at the same values of φ. We also show a zoom around one of the topological defects shown in the left panel, together with the theoretical calculations using the elastic theory, which produces the curves of director orientations.

In Fig. 29 (left panel) we show the fields $Q_2(\boldsymbol{r})$ (uniaxial nematic order parameter) and $Q_4(\boldsymbol{r})$ (tetratic order parameter) using a color scale for two different values of packing fractions $\eta = \varphi = 0.70$ and $\eta = 0.75$ used in the experiments. We can see that at the center of the cavity the uniaxial nematic ordering for both values of η is rather low while the tetratic one is relative high, indicating the presence of two equivalent directors along which the cylinders align. This tetratic phase in turn was shown to be stable at bulk from our scaled particle theory calculations as it wa shown above. But the most important fact is the presence of four defects, the relative small zones where the values of $Q_4(\boldsymbol{r})$ is depleted. Note that they are approximately positioned at the vertexes of an inscribed square. Moreover in the same figure is shown a zoom around one of these defects. If we trace out a line joining the rectangles of same color around the defect we produce a curved triangle which coincides with the director field lines produced within the elastic theory explained above. These facts show that despite the granular and nonequilibrium nature of our system this simple theory qualitatively explain the experimental results, in particular those regarding the presence of topological defects due to the orientational frustration of particles confined in into a disk. Thus our granular monolayer, in certain sense, can be assimilated to an equilibrium two-dimensional hard rectangle liquid-crystal fluid. In the right panel of the same figure we show the results form MC of the equilibrium thermal fluid of hard rectangles at the same values of packing fractions η. Note the similarities between experiments and simulations, with the same symmetry of the liquid-crystal texture at the center of the cavity and the presence of four point-like defects at the perimeter of the disk.

To end this section we present the experimental results on the vertically vibrated monolayers of granular triangular prisms [23]. The cross-section of the prisms are equilateral triangles of side 4 mm while their thickness is 1 mm. A total amount of approximately 3000 prisms are shaken in vertical direction with the same amplitude and frequency mentioned above. As we have already pointed out the stable uniform liquid-crystal phase of equilateral triangles is the 6-atic phase, with the orientational distribution function invariant under $\pi/3$ rotation, $h(\phi) = h(\phi + \pi/3)$. As we have shown before the elastic theory predicts that a 6-atic liquid crystal confined inside a disk, a geometry which frustrates the 6-atic ordering, under the assumption that all topological defects are equivalents, predicts a total amount of 6 defects (with topological charges $q_i = +1$) positioned close to the vertexes of an inscribed hexagon. This prediction is totally corroborated by experiments, as can be seen from Fig. 30 (a) where we show the color-map of the order parameter fields $Q_{2n}(\boldsymbol{r})$ ($n = 1,2,3$). As expected the unique order parameter with high enough values is that corresponding to the 6-atic symmetry, $Q_6(\boldsymbol{r})$, which at the center of the cavity reaches its maximum value. Six point-like defects (regions where $Q_6(\boldsymbol{r})$ is depleted) are positioned at the cavity walls close to the vertexes of an hexagon, as the theory predicts. Moreover if we compare the curves tangents to the 6-atic directors, as obtained from the elastic theory, are similar to the contour plots of the $Q_6(\boldsymbol{r})$ field around any defect (see the zoom of a defect from panel Fig. 30(a)). Again, MC simulations of the of the confined hard equilateral triangle fluid at equilibrium confirm the same qualitative results (see panel (b)).

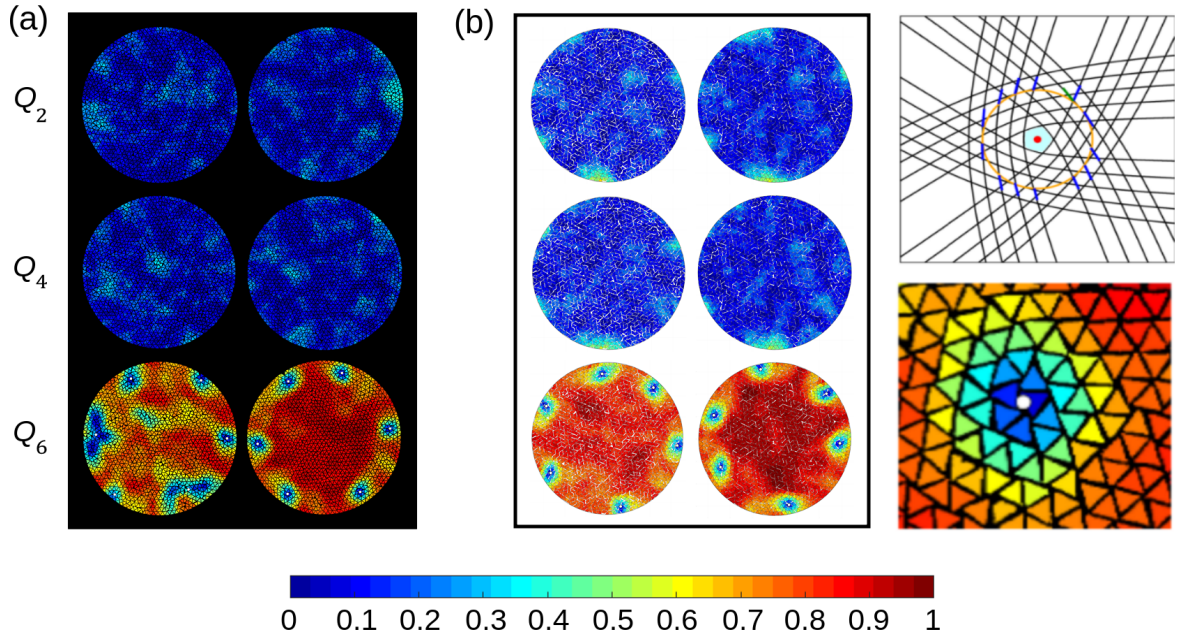


Figure 30: (a): Color map of the order parameter fields $Q_{2n}(\boldsymbol{r})$ ($n = 1,2,3$) of vertically vibrated monolayers of triangular prisms confined in a circular cavity of dimension 15 cm. The fixed values of packing fraction are $\eta = 0.78$ (left) and 0.85 (right). (b): The same fields obtained from MC simulations of equilibrated hard equilateral triangle fluid confined inside a disk of same dimension. We show a zoom of one of defects of panel (a) together with the elastic theory calculations of the curves corresponding to the 6-atic director orientation field.

References

[1] L. Mederos et al., J. Phys.: Condens. Matter **26**, 463101 (2014).

[2] Y. Rosenfeld, Phys. Rev. Lett. **63**, 980 (1989).

[3] J. M. Meijer et al., Phys. Rev. B **86**, 064303 (2012).

[4] A.-P. Hynninen, J. Chem. Phys. **131**, 064902 (2009).

[5] E. Velasco et al. Phys. Rev. E **60**, 3158 (1999).

[6] M. Dijkstra, R. van Roij and R. Evans, Phys. Rev. E **59**, 5744 (1999).

[7] C. Tschierske, Angew. Chem. Int. Ed. 52, 8828 (2013).

[8] P. Bolhuis and D. Frenkel, J. Chem. Phys. **106**, 666 (1997).

[9] L. Onsager, N. Y. Acad. Sci. **51**, 627 (1949).

[10] D. Frenkel and B.M. Mulder, Mol. Phys. **55**, 1171 (1985).

[11] J. A. Anderson et al., Phys. Rev. X **7**, 021001 (2017).

[12] R. Evans, *Density functionals in the theory of nonuniform fluids*, pp. 85 in *Fundamentals of inhomogeneous fluids*. ed. D. Henderson, CRC Press (1992).

[13] T. K. Vanderlick, H. T. Davis, and J. K. Percus, Phys. Rev. A **39**, 2422 (1989).

[14] J. A. Cuesta and Y. Martínez-Ratón, Phys. Rev. Lett. **78**, 3681 (1997).

[15] P. Tarazona, Phys. Rev. Lett. **84**, 694 (2000).

[16] H. Reiss, H. L. Frisch, and J. L. Lebowitz, J. Chem. Phys. **31**, 369 (1959).

[17] J. Martínez-Ratón, E. Velasco, and L. Mederos, J. Chem. Phys. **122**, 064903 (2005).

[18] Y. Martínez-Ratón, E. Velasco, and L. Mederos, Phys. Rev. E **72**, 031703 (2005).

[19] D. de las Heras, Y. Martínez-Ratón, and E. Velasco, Phys. Rev. E **76**, 031704 (2007).

[20] Y. Martínez-Ratón, A. Díaz-De Armas, and E. Velasco, Phys. Rev. E **97**, 052703 (2018).

[21] F. Frank, Discuss. Faraday Soc. **25**, 19 (1958).

[22] M. González-Pinto, F. Borondo, Y. Martínez-Ratón, and E. Velasco, Soft Matter **13**, 2571 (2017).

[23] J. Vega, E. Velasco, and Y. Martínez-Ratón, Phys. Rev. Research **7**, 043238 (2025).